The role of river discharge and geometric structure on diurnal tidal dynamics, Alabama, USA

S. L. Dykstra[1,2,3*], B. Dzwonkowski[2,3], and R. Torres[1]

[1]School of Earth, Ocean, and Environment, University of South Carolina, Columbia, SC 29208.

[2]Department of Marine Sciences, University of South Alabama, Dauphin Island Sea Lab, Dauphin Island, AL 36528.

[3]Dauphin Island Sea Lab, Dauphin Island, AL 36528.

Corresponding Author: Steven L. Dykstra (stevenldykstra@gmail.com)

Key Points:

- Along the fluvial-marine transition, river discharge attenuated tides in landward regions and amplified tides in seaward regions
- The landward most location of tidal flow reversal (flood limit) shifted longitudinally ~180km with unsteady river discharge
- Planform channel geometry may not be a robust indicator of the transition in tide-river hydrodynamics

Key Words: fluvial-marine, Mobile Bay, longitudinal, geomorphology, tidal river, estuary

Abstract

As tides propagate inland, they become distorted by channel geometry and river discharge. Tidal dynamics in fluvial-marine transitions are commonly observed in high-energy tidal environments with relatively steady river conditions, leaving the effects of variable river discharge on tides and longitudinal changes poorly understood. To study the effects of variable river discharge on tide-river interactions, we studied a low-energy tidal environment where river discharge ranges several orders of magnitude, the diurnal microtidal Tombigbee River-Mobile Bay fluvial-marine transition, using water level and velocity observations from 21 stations. Results showed that tidal attenuation was reduced by the width convergence in seaward reaches and height convergence of the landward backwater reaches, with the channel convergence change location ~40-50km inland of the bayhead and seaward of the largest bifurcation (~rkm 90-100). River events amplified tides in seaward regions and attenuated tides in landward regions. This created a region of river-induced peak amplitude seaward of the flood limit (i.e., bidirectional-unidirectional current transition) and passed more tidal energy inland. Tidal currents were attenuated and lagged more with river discharge than water levels, making the phase lag dynamic. The river impacts on the tides were delineated longitudinally and shifted seaward as river discharge increased, ranging up to ~180 km. Results indicated the location and longitudinal shifts of

river impacts on tides in alluvial systems can be estimated analytically using the ratio of river discharge to tidal discharge and the geometry convergence. Our simple analytical theory provides a pathway for understanding the tide-river-geomorphic equilibrium along increasingly dynamic coasts.

Plain Language Summary

Coastal cities and ports are commonly affected by tides and rivers, concentrating industry, infrastructure, and economies in complex regions where tide-river interactions affect flooding, erosion, and water quality. Tide-river interactions are commonly studied in stable rivers with large tides, limiting the variability of tide-river interactions, leaving the effects of river discharge on tides poorly understood, and the risks for coastal communities during large river discharge events difficult to determine. To study the effects of river discharge on tide-river interactions, observations in Alabama were investigated, spanning the Tombigbee River through Mobile Bay to the Gulf of Mexico. Results show that channel geometry and river discharge affected the shapes of tides. As river discharge increased, the tidal-dominated region shifted up to 180 km seaward (110 miles) and became river-dominated. The shift was captured in a simple equation using the river-tidal energy ratio and generalized geometry, suggesting the shift increases with the range of river discharge and that the greatest flooding and erosion risks to coastal communities can sometimes be the sea and other times rivers. This simple equation provides a new tool for managers to understand tide-river interactions now and under future changes from human development and sea level rise.

1 Introduction

Most ports and mega cities are located where rivers reach the sea, concentrating the human population, economies, and infrastructure in regions where water levels and currents are controlled by rivers and tides. These fluvial-marine transitions extend far inland to the head of tides O(10-1,000 km), connecting the land to the sea and forming critical links for biogeochemical cycles, source to sink sediment dynamics, and ecosystems. Most organisms consumed as seafood spend at least part of their lifecycle in this transitional environment (Gunter 1974). Tide and river dynamics are described analytically based on their geometries and are highly variable, changing on timescales of hours to days. When tides and rivers interact, the processes are strongly nonlinear, and shape the local channel or estuary geometry (Dalrymple & Choi 2007; Haigh et al. 2020; Sulaiman et al., 2021). The complex nature of tide-river-geomorphic interactions are still poorly understood despite their importance to human society.

Tides are generated by astronomical forces and propagate as long waves through the ocean. Tidal waves are orbital, like wind waves, with a vertical component observed in water level and a horizontal component observed in currents. Tides can amplify or attenuate along coasts and enter confined bays and rivers as

forced waves (Friedrichs, 2010). The forced tidal waves become further modulated by landward decreasing cross-sectional areas, bed friction, and river flow. Therefore, modulation can make tidal currents more effective at scouring and transporting sediment, shaping their geomorphic environments, as well as mixing surface and bottom waters, which can reduce salt intrusion, oxygenate bottom waters, and bring nutrients to the surface (Dalrymple & Choi, 2007; Ralston & Geyer, 2019). Tides and their effects also are influenced by direct human impacts on the geometry (e.g. dredging, structures, reclamation; Winterwerp & Wang, 2013) and climate change (e.g. stratification, sea level rise; Talke & Jay, 2020). While semidiurnal tides often have larger amplitudes, some of the longest historical records and climate models show diurnal tides are amplifying faster and have experienced larger phase changes (Cartwright, 1971; Green, 2010). If these trends continue, regions will become more diurnal and similar to the modern diurnal areas of the western and south Pacific Ocean, the west coast of Australia, and the Gulf of Mexico/Caribbean Sea.

The transition from tidal to river dominant flow creates a large change in the equilibrium geometry of fluvial-marine transitions (Wright et al., 1973; Sassi et al., 2012; Kästner et al., 2017). Tidally dominated areas are similar to the sea, wide and flat. For tidal dominated areas in alluvial systems at geomorphic equilibrium, the width converges landward forming a trumpet shape and the shallowest region is a bar at the mouth (Figure 1a; Friedrichs & Aubrey, 1994; Valle-Levinson et al., 2019; Dronkers, 2017; Kästner et al., 2017). These reaches can be open bays, divided into multiple deltaic distributaries, or a combination of both (e.g., bayhead delta; Dalrymple & Choi, 2007). River dominated regions are similar to low lying fluvial environments, relatively narrow and sinuous. At equilibrium, the depth is variable like inland reaches, but increases seaward, forming a backwater environment where the riverbed drops below sea level (i.e., M1 hydraulics; Chow, 1959) (Figure 1b). The diverging bed and water surface decreases river flow and sediment transport, increasing deposition and river sinuosity (Ganti et al., 2019; Lane, 1957; Lazarus & Constantine, 2013; Myrick & Leopold, 1963). These reaches are dominated by tidal freshwater forest wetlands, which can affect the morphodynamics and on the US east coast alone account for 2,850 km of waterways (Ensign & Noe, 2018). It has been reported that where the tide and river dominated reaches meet is the deepest region of the fluvial-marine transition and has little change in cross-sectional area (Gugliotta & Saito 2019; Kästner et al. 2017).

Fluvial-marine transitions have flow contributions from each end with peak tidal currents decaying in a landward direction and river currents decaying in a seaward direction. The balance point occurs where flood tides are no longer able to reverse river flow and is herein called the flood limit (Figure 1c). The flood limit commonly delineates analytical solutions into the bidirectional flowing tidal estuary (herein estuary) and the tidal river, where unidirectional flow is tidally modulated (e.g., Jay & Flinchem, 1997; Friedrichs, 2010; van Rijn, 2012; Cai et al., 2014). The landward extent of the tidal river is the tidal limit, where the incident tidal wave at the mouth has fully decayed (Figure 1c). The tidal

and river current rates of decay can affect each other, creating complex interactions. Tide-river interactions may change with tidal variability, which can range several fold over spring-neap cycles, but river discharge often has a larger range, up to several orders of magnitude, making tide-river interactions strongly dependent on river discharge.

Observations show inconsistent tidal responses to river events, amplifying tides in some locations and attenuating them in others. Studies capturing most of the spatial extent of a fluvial-marine transition, including those on the St. Lawrence (Godin, 1985, 1999; Matte et al., 2014), Mekong (McLachlan et al., 2017), Yangtze (Guo et al., 2015), and Guadalquivir River (Losada et al., 2017), generally show that terrestrial flood events amplify tides in seaward reaches and attenuate tides landward reaches, but do not delineate where this change occurs. While the mechanism causing these reach-specific tidal responses may not be identified, other studies indicate that river-associated-tidal-amplification is attributed to reduced friction. The reduced friction is caused by high stratification from large fluxes of freshwater, lowering the density of the surface layer, or more sediments, increasing the water density near the bed (Talke et al., 2009; Díez-Minguito et al., 2012a). River-associated-tidal-attenuation is attributed to high friction from the river flow and the added river-tide interaction (Buschman et al., 2009; Godin, 1985; Kästner et al., 2019).

1.1 Tide-River-Channel Interactions

River processes interact with the geomorphology and are self-organizing, reshaping their geometries toward equilibrium (e.g., Leopold et al., 1964; Phillips & Jerolmack, 2016), similar to tide-geomorphic interactions (Dronkers, 2017). For example, in alluvial estuaries, the tidal energy loss from friction is balanced by width convergence (e.g., Figure 1a), causing partial reflection of the tidal wave. When the tidal amplitude is constant across the reach, the phase lag is ~45 degrees (i.e., phase difference of horizontal and vertical tidal components); this is called an *ideal* estuary. If friction dominates, the estuary is hyposynchronous and causes the wave to attenuate, the phase lag to decrease, and the phase and wavenumber to increase. If convergence dominates, the estuary is hypersynchronous and causes the wave to amplify, the phase lag to increase, and the phase and wavenumber to decrease (Friedrichs, 2010; Friedrichs & Aubrey, 1994). Estuarine convergence in new empirical relationships is shown to decrease for systems with higher river discharge, due in part to the larger river width, indicating that estuarine morphology and tides reach an equilibrium that may change with river discharge (Dronkers, 2017; Leuven et al., 2018).

Tide and river processes are also interpreted from geologic records from depositional patterns, bedforms/structure, and trace fossil assemblages (Davis, 2011; Sisulak & Dashtgard, 2012; van den Berg et al., 2007). Stratigraphic reconstructions (e.g., facies) capture the longitudinal change of fluvial-marine transitions, but some regions have complex alternating patterns that suggest reaches cyclically switch between river and tidal dominant environments (Davis, 2011; Rossi

et al., 2017). Dalrymple et al. (2015) hypothesize the alternating patterns are caused by tide-river processes shifting seaward and landward with the rise and fall of river discharge. However, longitudinal shifts are poorly documented in modern equivalent systems, leaving the hypothesis unsubstantiated (Dalrymple et al., 2015).

1.2 Motivation for New Observations

Longitudinal changes in tidal dynamics are not commonly translated from river induced tidal attenuation and may be a result of small observed changes due to previous literature focusing on similar systems (i.e., macrotidal/mesotidal, semidiurnal) with small ranges in river discharge (e.g., an order of magnitude or less). The ratio of river discharge to tidal discharge ($Q_{rf} = Q_r/Q_t$) is relatively stable, making tide-river interactions and their geomorphic effects also stable (Zhou et al., 2014). Thus, studies on river induced tidal attenuation often ignore the effects of discharge changes (e.g., Horrevoets et al., 2004). In contrast, recent observations of the microtidal Kapuas River (tidal range 0.35-1.35m) show an order-of-magnitude increase in discharge causes strong tidal attenuation and shifts the tidal limit over 130km seaward (Kästner et al., 2017). The tidal period also strongly affects wave energy. The dominant tidal specie (e.g., diurnal (D1), semidiurnal (D2)) strongly affects the tidal friction of all species, making D1 tidal attenuation in semidiurnal environments very complex and poorly understood (Godin, 1985; Jay & Flinchem, 1997). For simplicity, tidal theory is often derived explicitly for D2 waves (e.g., van Rijn, 2012; Winterwerp & Wang, 2013), limiting theory for diurnal environments and may partially explain why there are no studies of tide-river interactions in diurnal systems.

An advanced understanding of tidal and river hydrodynamics is also limited by studies that principally rely on water level observations (e.g., Jay et al., 2015; Webb & Marr, 2016). This is problematic because water level only captures the least complicated vertical component of the tidal wave. For discharge/currents, friction, and transport, the horizontal wave component, captured with velocity observations, is needed. Horizontal waves can theoretically be estimated with water levels, although this estimation assumes that the vertical and horizontal waves are congruent and temporally offset with a constant phase lag (Sassi & Hoitink, 2013; Buschman et al., 2009), which may not be appropriate for many realistic environments (Friedrichs, 2010). In width-converging environments, the convergence rate is positively related to the vertical amplitude and inversely related to the horizontal amplitudes (Friedrichs, 2010). For height-convergent environments, new theory shows that river discharge attenuates horizontal waves faster than vertical waves, making horizontal-vertical wave relationships very complex (Kästner et al., 2019). Direct observations of horizontal and vertical waves in the Guadalquivir River show river events can strongly affect phase lag (Díez-Minguito et al., 2012a; Losada et al., 2017). This notwithstanding, very few fluvial-marine transitions have long-term velocity observations at multiple locations, leaving a large gap in our understanding of

horizontal wave propagation.

The purpose of this study is to quantitively assess tidal attenuation dynamics in the fluvial-marine transition. Thus, we hypothesize: tide-river longitudinal shifts in a fluvial-marine transition are caused by variable river discharge (i.e., Dalrymple et al. 2015). Our objectives are to 1) observe river discharge and geometry affects on the longitudinal variability of tides (vertical and horizontal components), 2) analytically capture longitudinal shifts of tide-river interactions, and 3) identify how diurnal tides may affect hydrodynamics and geomorphology different than semidiurnal tides. Objectives are completed using long-term water level and velocity observations, spatial data (e.g., LiDAR), and analytical equations to capture the dynamics of a diurnal microtidal environment, the Mobile Bay-Tombigbee River fluvial-marine transition in Alabama, USA.

2 Theory

Tidal waves propagating along a fluvial-marine transition are primarily modulated by friction, basin shape, and subtidal flows, which generally arise from geomorphic and river discharge interactions. The primary geomorphic effects on tides are bed stress, reflectance (e.g., convergence, dam), and resonance (Jay, 1991; Friedrichs, 2010). The primary river effects on tides are through river currents (e.g., friction), the discharge volume (e.g., reduces tidal prism), and density (e.g., stratification) (Cai et al., 2014).

2.1 Tidal Controls on the Morphology of *Ideal* Estuaries

For tide-geomorphic interactions, convergence is found using an e-folding length based on the reach width (w) or height (h):

$w = w_0 e^{-x/L_w}$ (Equation 1a)

$h = h_0 e^{-x/L_h}$ (Equation 1b)

where L_w is the width e-folding length, L_h is the height e-folding length, and the subscript of 0 indicates the longitudinal location inland where landward convergence begins. This location may be offset from the estuary mouth (e.g., bar-built estuary; Dronkers, 2017). As the e-folding length increases, convergence decreases. The area (a) e-folding length can be solved following van Rijn (2011):

$L_a^{-1} \approx L_w^{-1} + L_h^{-1}$ (Equation 2)

The e-folding length is used to quantify the role of convergence on tidal amplitude following Talke & Jay (2020):

$\eta(x) \approx \eta_0 e^{\,x}$ (Equation 3a)

where

$\mu \approx \frac{1}{2L_a} - \omega\sqrt{c_d \eta_0 L_p}/\sqrt{gh^3}$ (Equation 3b)

Here, x is the along channel distance inland, is the damping rate, is the angular frequency (i.e. =2 /T, T is tidal period), c_d is the drag coefficient, is the vertical tidal amplitude, L_p is the length scale controlling the tidal prism, g is gravity, and h is height. The first term in the damping rate (Eq. 3b) is convergence and the second is the damping modulus. Equation 3 indicates the vertical tidal amplitude is a balance between convergence, amplifying the vertical tide, and friction, attenuating the tide.

In convergent estuaries, the vertical and horizontal tidal components are closely related through (Friedrichs, 2010):

$U_t = \frac{L_w}{h}\frac{w_b}{w}$ (Equation 4)

where w_b/w is the mean width (w_b) over a tidal cycle relative to the channel width (w). Equation 4 indicates tidal velocity, as a measurement of the horizontal tidal wave, is proportional to the vertical tidal amplitude, half the magnitude for diurnal tides, relative to semidiurnal tides, and inversely related to convergence (i.e., convergence is $1/L_w$). This inverse relationship occurs because convergence partially reflects the tidal wave, which, for the vertical tide that propagates as a transverse wave is in phase and adds to the amplitude, but for the horizontal wave which propagates as a longitudinal wave is out of phase and subtracts from the amplitude. Thus, tidal modulation may produce different results for the vertical and horizontal components.

When the estuary attains *ideal* geographic attributes at morphodynamic equilibrium and the tidal magnitude is constant, =0. Equation 3b can then be rewritten to find the morphodynamic equilibrium of an estuary based on the incident tidal momentum:

$\frac{\eta_0}{T^2} \approx \frac{h^3 g}{16\pi L_a^2 L_p c_d}$ (Equation 5)

where, the tidal properties are on the left side and the morphodynamics are on the right. Tidal period and magnitude are inversely related because longer periods have less energy. The tidal momentum scales positively with height and inversely with the length terms and drag coefficient, therefore, equation 5 shows that for a diurnal and a semidiurnal system of similar tidal magnitude, the diurnal system is longer.

The landward river dominated reach of fluvial-marine transitions are primarily affected by marine processes through sea level creating a backwater environment. Here, river flood waves make flow unsteady as the diffusive waves (i.e., pressure gradient-friction momentum balance) propagate seaward and become dynamic waves (i.e., pressure gradient-friction-acceleration balance) in the corresponding tidal dominated reaches (Dykstra & Dzwonkowski, 2020a). The river waves occur later in a seaward direction, like tides in a landward direction, making tide-river interactions along a longitudinal transect nonconcurrent. Assuming steady river discharge, Kästner et al. (2019) derives the first analytical solutions for tidal waves in backwater reaches, showing tidal waves are modulated by strong river currents and by river water level slope, making height convergence

dynamic. While analytical solutions for tidal wave-river wave interactions are still needed, our study provides an observational exploration of these complex processes.

2.2 The Longitudinal Variability of Tide-River Interactions

To delineate the tidal and river dominant reaches, Hoitink & Jay (2016) propose a novel method based on the temporal variability of water levels utilizing the nonlinaries of tide-river interactions. As tides are modulated by river discharge, they become asymmetric and transport water landward (e.g., Stokes transport). Larger tidal amplitudes transport more water. Due to spring-neap cycles, water is temporally stored in inland reaches, creating a subtidal setup with a fortnight period (e.g., Msf). Where the subtidal variability exceeds tidal variability, the lowest low water occurs during neap tides. With this method, the estuary ends and the tidal river begins where the lowest spring tide water levels become higher than the lowest neap tide water levels (Jay et al., 2015; Hoitink & Jay, 2016).

Instead of delineating with water level variability, the estuary-tidal river boundary can be delineated with flow direction as bidirectional or unidirectional at the flood limit. Due to the absence of salt at the flood limit, tidal phase and ebb-flood asymmetry have been reported as nearly uniform across the water column of a coastal plain river (Yankovsky et al., 2012), suggesting velocity measured at one location can be used to estimate the cross-sectionally averaged velocity and discharge. River discharge and peak tidal discharge (Q_t=$U_t$hw, where U_t is the cross-sectionally averaged peak tidal velocity) can then be used with mass conservation to simulate the longitudinal variability of the flood limit in an *ideal* estuary (i.e., constant tidal amplitude) when convergence is known (Eq. 1):

$x_{\mathrm{rf}} = -L_w \log\left(\frac{Q_r}{w_0 h U_t Q_{\mathrm{rf}}}\right)$ (Equation 6a)

where x_{rf} is the longitudinal location of a given river discharge fraction (Q_{rf}=Q_r/Q_t) such as the flood limit (Q_{rf}=1) or location where river flow has negligible tidal damping effects (Q_{rf}=4/3 0.42; Kästner et al. 2019). Equation 6a can be simplified for area using Equation 2:

$x_{\mathrm{rf}} = -L_a \log\left(\frac{Q_r}{a_0 U_t Q_{\mathrm{rf}}}\right)$ (Equation 6b)

Or, if U_t is unknown and intertidal effects are negligible (i.e. w_b/w 1), substituting in Equation 4:

$x_{\mathrm{fl}} = -L_w \log\left(\frac{Q_r}{w_0 \ L_w Q_{\mathrm{rf}}}\right)$ (Equation 6c)

Equation 6c shows the longitudinal location of the flood limit has a geomorphic control, largely set by the mouth width and convergence, and can dynamically change with river discharge and tidal amplitude. The log relationship suggests as river discharge increases by one order of magnitude the tide-river interactions will shift two e-folding lengths seaward.

3 Data and Methods

3.1 Data Sources

Long-term publicly available monitoring records were the original source of all data used (Figure 2, table S1). Most water level, velocity, and river discharge data were accessed from Dykstra & Dzwonkowski (2020b) and updated through May 2020. The 21 stations used in this study were labeled with the first letter representing the body of water (e.g., G:Gulf, B:bay, D:delta, R:river) followed by the along channel distance inland from Main Pass along the longitudinal transect. Stations not on the longitudinal axis are to the east and are noted with an E (e.g. D96E). Data from D100 and stations landward were accessed from the USGS (waterdata.usgs.gov/nwis) while the stations seaward were accessed from NOAA (tidesandcurrents.noaa.gov) and the Alabama Real-Time Coastal Observing System (ARCOS; arcos.disl.org) except for B8, which was from the USGS. Most stations had a sampling interval between 6 and 60 minutes.

To put station data were in similar terms, all water levels were put on the common vertical datum NAVD88. Current velocities were determined from acoustic Doppler current profilers (ADCP) orientated vertically (G-14, B23) or horizontally (B47, D53, D100) as well as a benthic acoustic stress sensor (B8). To minimize differences between collection methods for the horizontal and vertical oriented ADCPs, only bins between one-quarter and one-third of the upper water column were used. This vertical bin range overlaps with the index velocity of the horizontal sensors as determined by the source organization (e.g., Ruhl & Simpson, 2005). The primary flow axis was determined by the major tidal harmonic axis (K1 & O1) with t_tide (Pawlowicz et al. 2002). For the Gulf of Mexico station (G-14), the major tidal axis was inline with the shipping channel, following the longitudinal axis. Because the extensive data was averaged (described below), non-tidal shelf circulation was not removed (e.g., inertial oscillations). While some data do not temporally overlap, all measurements could be referenced to discharge during a period without bathymetric changes in dredging or the construction of bridges or upstream dams. Specific details of data sources, length of records, and sensors used at each station is in the supplemental material (Table S1).

Local ground surface elevations were taken from USGS 3DEP Lidar (USGS, 2016, 2020), The Shuttle Radar Topography Mission (Farr et al., 2007), a NOAA DEM (NOAA National Geophysical Data Center, 2009), and Dykstra & Dzwonkowski (2020b). For topography, Lidar was converged to a 10m DEM using Opentopography. For bathymetry, the NOAA DEM was used to analyze the bay geometry, but had a limited spatial extent and missing data in the mid delta. Thus, landward of the bayhead, depth and area of the Mobile and Tombigbee Rivers were calculated using a DEM of the longitudinal channel from Dykstra & Dzwonkowski (2020b). No comparable data of the Tensaw could be acquired. Channel width was measured every 2km and included all five major anastomosing channels of the Tensaw distributary (i.e., Tensaw, Blakely, Apalachee, Raft,

and Middle Rivers). Because the Middle River regional avulsion was half the length of the Tensaw, Middle River widths were measured at a 1km interval. Sinuosity was calculated by dividing the centerline length by the length of a low-passed centerline using a 10km-moving mean, the bin size revealing highest mean sinuosity.

Timeseries Analysis

The water level and velocity timeseries for each station was analyzed for changes with river discharge and compared to reveal spatial variability, shown in river discharge-longitudinal space. Because tide-river interactions along a longitudinal transect are nonconcurrent, for each station, river discharge was temporally offset from upstream observations following Dykstra & Dzwonkowski (2020a) and tidal observations were related to the mouth (B0) after being offset by the observed lag time (see continuous wavelet transformations below). Capturing longitudinal changes from river discharge was first done to delineate the estuary and tidal river using methods based on water level or velocity observations (e.g., Hoitink & Jay, 2016). Neap and spring periods were determined from B0 tidal amplitudes (i.e., K1-O1 beat) using the first and fourth quartiles, respectively. After being temporally lagged for each station, the lowest water level for every neap and spring period was identified. Instead of bulk averaging the entire timeseries, they were sorted by river discharge and averaged using a moving-mean. Because station timeseries were different lengths, the box size was determined using 10 degrees of freedom (i.e., n/10). Then spring means were subtracted from neap means. Results from each station were linearly interpreted longitudinally, revealing changes in discharge-longitudinal space. The velocity method found the flood limit where the peak spring flood was zero. Peak spring floods were found by first identifying velocity amplitudes at each station using band-passed time series (3–40-hour Lanczos filter; e.g., Dzwonkowski et al., 2015), for amplitudes>2cm, periods of 24.8±2 hours, and removing outliers (Figure S1a). The corresponding non-filtered values were the peak flood velocities (Figure S1b). To estimate spring flood velocities, the sinusoidal spring-neap relationship was utilized as sinusoidal functions have standard deviations $\sigma(\eta) = \eta/\sqrt{2} \approx 0.71\eta$ (η is amplitude), allowing $\overline{\eta} + \sigma$ to represent the 71^{st} percentile. After being sorted by river discharge, moving-means and moving-standard-deviations were taken of peak flood velocities using a window size of 31, and added (Figure S1b). Like the water level method, results from each station were linearly interpreted longitudinally.

Continuous wavelet transformation was used to detect relative tidal amplitudes and relative tidal phases in a time-frequency domain (Jay & Flinchem, 1997). Following previous tidal applications, the toolbox of Grinsted et al. (2004) was utilized with a Mortlet-type wave and a non-dimensional frequency scale of 6 (e.g., Sassi et al., 2013). This method calculates energy as a wavelet power spectrum, wavelet cross correlation between stations, and significance for both at a 95% confidence interval. Because the long timeseries of water level measure-

ments at the mouth (D0; 38 years) were concurrent with all other observations, water level and velocity were normalized to the mouth water level observations. This was done using the wavelet cross correlation to capture relative phase in the water level and velocity. For relative amplitude, the relative phase was used to offset the significant wavelet power spectrum of each station before dividing it by the wavelet power spectrum from the mouth.

For the tidal phase lag (; i.e., phase between velocity and water level), a wavelet cross correlation was conducted where nearby water level and velocity measurements were available. Because the phase lag near the mouth (B8) was stationary (relatively insensitive to river discharge), the velocity phases relative to D0 water level were corrected with a constant offset. The offset was based on the phase lag (79.8 degrees, 5.50 hours) of near surface currents (-4m) in Main Pass from a short deployment (~3 months). For the local wavenumber (k), the wave frequency was divided by the celerity (c), calculated from the phase difference between two stations (i.e., k= /c).

4 Site Description: Tombigbee River-Mobile Bay Fluvial-Marine Transition

The Tombigbee River-Mobile Bay system in coastal Alabama provided a unique opportunity for this study with a high concentration of long-term datasets in a representative system (Figure 1, table S1). The flat shallow bay is a bar-build drowned valley estuary, 48 km long, averages 3.5m deep (NOAA National Geophysical Data Center, 2009), and is highly stratified throughout much of the year (Schroeder et al., 1990). River discharge entering Mobile Bay comes primarily from the Tombigbee and Alabama Rivers (watershed area: 51,921 and 58,896 km^2, respectively). Their mean river discharge is nearly the same and together form fourth largest coastal river discharge in the continental United States (1,866 m^3s^{-1}; Dykstra & Dzwonkowski, in-review). River discharge ranges from almost no flow (100 m^3s^{-1}), making it like a tidal lagoon, to large events (15,000 m^3s^{-1}) with magnitudes exceeding low flow on the neighboring Mississippi River (Dzwonkowski et al., 2018).

On the marine side, in the Gulf of Mexico, the natural period of oscillation is near resonance for diurnal tides, which nearly cancels semidiurnal harmonics and makes tides near Main Pass of Mobile Bay strongly diurnal (form factor>10) (Figure 1). The largest harmonics near Main Pass, K1 and O1, have equivalent velocity amplitudes and nearly equivalent water level amplitudes (13.4 cm and 14.3 cm, respectively; Seim et al., 1987), which creates a fortnight tropic-equatorial cycle (herein spring-neap) ranging ~0 to 60 cm. When the largest harmonics cancel, they form *dodge* tides as seen in Spencer Gulf, Australia (Nunes & Lennon, 1986), where the system becomes almost nontidal during neap periods. The diurnal tides are affected by river discharge in Main Pass where ebbing flow pulses large estuarine-river plumes into the Gulf of Mexico (Greer et al., 2018). A smaller fraction of Mobile Bay estuarine water exchanges through the other inlet, Pass aux Herons, into Mississippi Sound (0.36; Kim & Park, 2012).

At the bayhead is a delta (2,010 km^2) with five distributaries called the Tombigbee-Alabama Delta (Figure 2). The subaerial delta extends ~95 km to the Suwanee-Wiggins suture within a broad (10~20km) pre-Holocene valley (Greene et al., 2007). Four distributaries merge into the anastomosing Tensaw River, which has a local avulsion called Middle River that is notable for being wider and half the length of the parallel 24km Tensaw reach. The other major distributary is the Mobile River, which extends along the west side of the delta from the port city of Mobile to the Mobile-Tensaw Bifurcation (rkm 112). The Mobile distributary is only 1km shorter than the Tensaw mainstem, but generally receives two-thirds of the river discharge and has higher water levels (Robinson et al., 1956; Dykstra & Dzwonkowski, 2020a). This lower delta region is known locally as the Mobile-Tensaw Delta and is the most biodiverse location in temperate North America, earning a designation as the Mobile-Tensaw River Bottomlands National Natural Landmark (Waselkov et al., 2016). The Mobile River continues 9.5 km to the Tombigbee-Alabama River confluence (rkm 122). The landward single stem rivers have pronounced meander scrolls across the wide upper delta, suggesting strong fluvial influence and high morphodynamic activity (Smith, 1997). Because hydroelectric power peaking on the Alabama River (R238E) created interference with tides in upstream reaches, the longitudinal transect only continues up the Tombigbee River. The Tombigbee River extends beyond the delta apex (rkm 194) through a confined valley (~1km wide floodplain) to the downstream most point of flow regulation at the Coffeeville Lock & Dam (rkm 238).

4.1 A Quantification of System Geometry

With single strand rivers, a large delta (2,010 km^2; Dykstra & Dzwonkowski 2020a), and a bay, the fluvial-marine transition had large geometric changes in width, height, and sinuosity (Figure 4). The largest change in width occurs at the bayhead, narrowing by an order of magnitude. For the entire bay, width convergence is much stronger than height convergence (L_w=38 km; L_h 200 km) because the mean depth decreases only in the upper bay (Figure 4b).

At the bayhead, the delta channels are wide and deep (Figure 4a, b). The total channel width converges landward to the Tensaw-Middle Bifurcation at rkm 107 (L_w=41 km). Further landward, through the Mobile-Tensaw Bifurcation to the dams, the width is nearly constant (~360m). Examining the Mobile and Tensaw channels independently shows nearly all width convergence is along the Tensaw channels (L_w=33). The Mobile distributary width and depth significantly change further seaward (rkm 79 to 86), near the I-65 Bridge, quickly narrowing from a mean of 300 to 190m and deepening from a mean of -6 to -13m. For low river discharge conditions, when water levels are low, height convergence is much stronger than width convergence to the bridge (L_h=51 km; L_w=210 km) and landward along the Tombigbee River to the dam (L_h=159 km; L_w=421 km). Using L_h and L_w to solve for area convergence (Eq. 2) estimates the bay area e-folding length as 31km, the same as observing the bay

area convergence directly (Figure S1) and is nearly the same as the estimate for the lower delta channels (L_a 30 km).

Like convergence, sinuosity also changed in the delta (Figure 4c). Along the Mobile and Tensaw Rivers, sinuosity exceeded 2.5 in some locations and the upper delta landward of rkm 96 was on average significantly higher (1.8; $p<0.01$) than the other regions of the system. The elevated region of sinuosity reflects the commonly observed strait-meandering-strait planform of fluvial-marine transition geomorphology (Dalrymple & Choi, 2007) and the sinuosity change occurring inland of a width and depth change is consistent with observations in tide-dominated deltas (e.g., Fly, Yangtze, Irrawaddy; Gugliotta & Saito, 2019), even though the system is microtidal.

5 Results

5.1 Delineating the Estuary and Tidal River using Tidal Variability

Within the convergent geometry, water level and velocity throughout the system were primarily influenced by tides and river discharge, generating notable variability in the time series (Figure 5). To demonstrate the variability, we focus on the year 2010, a representative year with several discharge events in the winter and spring followed by a dry summer and fall (Figure 5a). River discharge ranged 130-8,600 m^3s^{-1} with large events lasting 1-4 weeks. Terrestrial runoff events caused the greatest variability at the landward stations (Figure 5b). At the seaward most stations (B0 and D52), water level variability was primarily tidal with fortnight modulation. When river discharge and water levels were low, a fortnight modulation was visible at all stations, even at R194 where tidal amplitude was smallest.

Velocity was also strongly influenced by river discharge and tides. Discharge events caused strong non-tidal seaward flows at the most landward velocity station (D100). Further seaward (B0, D53), velocity variability was primarily tidal with fortnight modulation, reflecting water levels and shelf currents (G-14). When river discharge was low, bidirectional tidal currents were observed at all stations. When river discharge was high, the fortnight modulation appeared noisier in velocity than water levels.

To identify if the tide-river interactions are occurring in the estuary or tidal river, the system is delineated for river discharge conditions ranging three orders of magnitude. At low discharge, low neap water was much higher than low spring water in most of the system (>10cm), suggesting estuarine conditions (e.g., Hoitink & Jay, 2016), except far inland where low spring water was higher (Figure 6a). The switch occurred near the delta apex and is interpreted as the estuary-tidal river delineation. As river discharge increased, low spring water became similar to low neap water and then higher, switching in the middle of the delta at 1,300 m^3s^{-1} and bayhead at ~5,000 m^3s^{-1}. However, some areas

switched multiple times. A careful examination of the data did not reveal any artifacts, suggesting the method was inconsistent and unreliable.

Instead of using water level to delineate the estuary and tidal river, a different approach used velocity to delineate bidirectional and unidirectional flow by finding the flood limit with maximum velocity (Figure 6b). At low discharge, maximum velocities were positive at all velocity stations, and were strongest in the lower delta. As discharge increased, flood velocities decreased in the middle delta until the maximum velocity reached 0 ms^{-1} at 600 m^3s^{-1}, detecting the flood limit (Figure 6b, S1b). At this discharge, the maximum flood velocity began decreasing at the bayhead and increasing in the lower bay. At a higher discharge (~2,000-3,000 m^3s^{-1}), the flood limit was detected at the bayhead and the flood velocity became smaller across the bay, allowing the flood limit to reach the middle of the bay at high discharge (>5,000 m^3s^{-1}). These sequential observations and interpolations capture a consistent seaward shift of the flood limit with discharge, unlike the water level method (Figure 6a). Interestingly, at the median discharge (~1,000 m^3s^{-1}), the flood limit was at the major geometry transition of the Mobile Distributary (~rkm 80), where the system transitioned from being wide and shallow to narrow and deep (Figures 4, 6b).

5.2 Tidal Response to Discharge

5.2.1 Tidal Amplitude and Lag Time

The seaward shift of the flood limit by discharge suggests a dynamic tidal response, which is further investigated, first using water level observations to capture the vertical tide. At low discharge, the D1 vertical tide (D1) amplified in a landward direction, peaking at D100 at 1.5 times the amplitude of Main Pass (D1 $_0$; Figure 7a). D1 attenuated across the upper delta and then amplified again from the delta apex to the dam, reaching similar amplitude to D1 $_0$, but 238 km inland. As discharge increased, the most inland reaches at the delta apex and dam (R194, R238) quickly damped and became undetectable almost simultaneously. Further seaward, river discharge caused D1 to first amplify and then attenuate. Peak amplitude for the middle of the delta occurred at ~600 m^3s^{-1}, for the bayhead at ~2,000-5,000 m^3s^{-1}, and at higher discharges, for the middle of the bay. Interestingly, peak amplitude for each region occurred further seaward as discharge increased.

Given the large amplitude changes with discharge, tidal phase and celerity is also investigated, using a time lag relative to Main Pass (Figure 7b). D1 vertical lag times (D1 $_t$) increased in a landward direction, though the distance traveled each hour was not consistent. At low discharge, the lag time to the bayhead, delta apex, and dam (rkm 48, 194, and 238, respectively) was approximately 1, 11, and 11.5 hours, respectively, showing wave celerity was very fast across the bay and slowed across the delta before accelerating further inland. This also indicates the entire system captures approximately half the D1 wavelength. As discharge increased, lag times increased. The strongest responses to river

discharge were at the most landward reaches where lag times increased, shifting from 11-11.5 to 13-14 hours, at which point the tidal signal was attenuated. The bayhead and bay had weaker responses with notable lag time increases of ~30 minutes at 5,000 and 8,000 m^3s^{-1}, respectively.

The vertical tide response to discharge was similar to the response of the horizontal tide. The diurnal amplitudes of the horizontal tide ($D1_u$) were largest near Main Pass and the bayhead, where flow was constricted (Figure 7c). As discharge increased, $D1_u$ quickly decreased at the furthest inland velocity site, in the middle delta, faster than the vertical tide and without first peaking. $D1_u$ increased at the bayhead, peaking at ~2,000 m^3s^{-1}, and then decreased at higher discharge. Observable damping also occurred near the mouth and at G-14, 14 kilometers offshore in the Gulf of Mexico. Compared to D1 , $D1_u$ was more spatially variable and damped at a lower discharge.

The vertical and horizontal tidal components also showed some different lag time responses to discharge (Figure 7d). The diurnal horizontal tide lag time ($D1_{ut}$) increased seaward and with discharge like $D1_t$, but had longer lag times. This is most clearly seen at the bayhead, where the lag time for $D1_{ut}$ was approximately 3 times that for $D1_t$, indicating the celerity was a third of $D1_t$. At low discharge in the Gulf of Mexico (G-14), the currents lagged the mouth by ~1.5 hours, suggesting the surface currents were strongly influenced by estuarine exchange (e.g., tidal rectification at an inlet). As river discharge increased, the lag time decreased at G-14 and was nearly in phase with the mouth when discharge exceeded 2,000 m^3s^{-1}, indicating the effects of river discharge on tidal dynamics extended onto the shelf.

5.2.2 Tidal Wave Propagation- Wavenumber and Phase Lag

The spatial variability of tidal response to discharge suggests there were changes in waveform, commonly determined by frequency, wavenumber, and phase lag . Because forced tidal waves have consistent frequency determined by astronomical processes, we focus on changes in wavenumber and phase lag . First, examining the spatial variability of the D1 wavenumber, using the vertical tide, shows the wavenumber across the bay increased and then decreased, similar to the width (Figure 8a). Across the delta, the wavenumber also increased and then quickly decreased as the tide approached the dam, nearly matching the large upper bay values. As discharge increased, the wavenumber generally increased. One exception was in the bay, where the wavenumber decreased with discharge to 2,000 m^3s^{-1}, but above 5,000 m^3s^{-1}, the wavenumber increased with discharge. The general trend suggests the wavelength decreased landward and with river discharge, ranging from over 2,000 km in the bay at low discharge to as small as 300 km as high discharge damped the tide in the delta.

Responses to discharge in the D1 phase lag ($D1_\phi$) were evident in the differences of $D1_{ut}$ and $D1_t$ and are clearly captured in Figure 8b. Near Main Pass, at low discharge, near surface tidal currents phased 5.7 hours ahead of the water

levels, or 82 degrees. This $D1_\phi$ decreased landward to 2.7 hours (39°) in the middle of the delta. As discharge increased across the delta and bay, $D1_\phi$ increased, peaked, and decreased, ranging almost an hour (12-15°). At the Gulf of Mexico site (G-14), $D1_\phi$ greatly increased when discharge exceeded 5,000 m^3s^{-1}, reaching 6.2 hours (90°), and did not peak. Interestingly, peak $D1_\phi$ was detected in the middle and lower delta at approximately the same river discharge the flood limit was detected and the tidal amplitudes peaked.

6 Discussion

The small diurnal *dodge* tides traveled 238 km from the Gulf of Mexico to the Coffeeville Lock & Dam, forming the Tombigbee-Mobile Bay fluvial-marine transition. Even though the tidal amplitude could be the same at both ends of the transition, like the Hudson River (Ralston et al., 2019), along the transition, the waveform (amplitudes, lag times, phases, wavenumbers) was strongly modulated by geometry and river flow. The wide range of river discharge, spanning several orders-of-magnitude, allows us to separate tidal modulation of geometry from river effects and reveals feedbacks in river-tide-geomorphic interactions.

6.1 Longitudinal Shift of the Tide-River Interactions

6.1.1 Geometric Controls on Tidal Waves

For geometric effects on tides, the cross-sectional area gradually decreased in a landward direction with sudden changes in the width-depth ratio, forming distinct convergent environments. In the bay, convergence was primarily controlled by the width (L_a=31rkm). Despite the shallow environment, the fast-amplifying tidal wave and the associated phase lag suggest the bay is hypersynchronous. In the lower delta, width and height convergence together formed approximately the same area convergence as the bay (L_a 30rkm). The relatively consistent amplitude, wavenumber, and phase lag near 45 decrees suggest the reach is *ideal* with partial reflection and friction nearly balanced. Further landward was a backwater environment with weaker convergence primarily controlled by the height (L_a=115rkm). The slow attenuating tidal waves suggest the reach was hyposynchronous, except near the end where tidal waves may have reflected off the dam.

6.1.2 River discharge controls on tidal waves

Similar to the geometric modulation of the tidal wave, the waveform was also modulated by river discharge. The most consistent river modulation led to tidal phases (i.e., lag time from D1) and wavenumbers increasing with river discharge, indicating wave celerity and wavelength decrease with river flow, supporting analytical theory (e.g., Jay & Flinchem 1997, Kästner et al., 2019). The tidal amplitude and phase lag had two responses to river discharge, increasing and decreasing, that depended on the river magnitude. To clearly identify how river discharge affects tidal amplitude, the river discharges at which the tidal

amplitude peaks and damps are identified for each station (Figure 9). As discharge increased, each station had a common response: the tide first peaked in amplitude, followed by the flood limit, and then at higher discharges, the tide damped at the inland stations. Comparing stations longitudinally shows the pattern shifts seaward or landward as a function of discharge with high (low) discharge shifting responses seaward (landward).

The location of the flood limit and peak tidal amplitude closely followed analytical solutions based on convergence length (Eq. 6b). Because area convergence changed in the middle of the delta, different solutions were used for seaward (L_a=31km, rkm 6-86) and landward reaches (L_a=115km, rkm 86-238; Figure 9). All four flood limit observations were within 10km of the analytical solved location for Q_{rf}=1, delineating the bidirectional estuarine currents (red shading) from the unidirectional tidal river. The location of D53, being seaward of the solution, likely resulted from the local Mobile Distributary area e-folding length being longer than the combined lower delta; causing the local cross-sectional area to be relatively smaller, forcing the flood limit further seaward. The peak tidal amplitude closely aligned with the analytically solved location for $Q_{rf} = 4/3$, delineating the landward region where river discharge would be expected to begin attenuating the tide (blue shading; Kästner et al., 2019). It also aligns well with the conditions at which river discharge is observed by Nobel et al. (1996) to increase subtidal bottom currents and bed friction (3,000 m^3s^{-1}, rkm 25). Deviations from the theoretically predicted locations of flood limit and peak tidal amplitude in the upper bay are likely a result of the bay being hypersynchronous and not having *ideal* geometry. By additionally including the observed salinity limit (5psu), we see it also moves seaward with river discharge and follows Q_{rf}=4/3 , suggesting the solution also captures estuarine flushing. By assuming some level of stratification seaward of the salinity limit, the Q_{rf}=4/3 point in the system appears to be the location at which the primary river discharge effect on tides is reducing friction through stratification, allow the tides to amplify. Landward of this point, river discharge would be expected to attenuate tides due to increased friction from strong flow velocities.

The simple analytical equation based on tide-geomorphic equilibrium (i.e., e-folding length) and conservation of mass captures tide-river interactions shifting seaward as river discharge increases (i.e., Equation 6b; Figure 9). For the weaker convergence of the inland backwater reaches, tidal-fluvial processes (e.g., tidal rivers) moved seaward much faster with river discharge. Within a constant region of area convergence, river discharge does not change the longitudinal length of any given tide-river interactions as they shift seaward (Figure 9). For example, the region where tides reverse and attenuate from river discharge does not change in size longitudinally (purple shading). This low energy region typically contains the turbidity maximum and can be difficult to identify because the tidal dynamics are poorly captured in analytical solutions (Figure 1c; Burchard et al., 2018; van Rijn, 2012; Jay & Flinchem, 1997). In Mobile Bay at rkm 20, a turbidity spike is observed when Q_r>5,000 m^3s^{-1} (~0.01 to 1 g/L; Ha & Park, 2012) and matches the predicted region of the turbidity maximum, sug-

gesting the simple solution may also be able to estimate the longitudinal shifts of estuarine sediment dynamics.

6.2 Reach Specific Tide-River-Geomorphic Interactions

6.2.1 The Transition from Tide to River Dominated Morphology

In the Mobile-Tombigbee fluvial-marine transition, the change from tidal-dominated to river-dominated morphology was gradual but had one region where the change was greatest. Assisted by a planview (e.g. Fig 2), the transition from river to marine dominated environments is commonly delineated at the bayhead with tidal influence reaching the Mobile-Tensaw bifurcation (e.g. Byrnes et al., 2010). Using width, depth, and area, our results suggest the bayhead transition to the delta does not significantly affect the total cross-sectional area or area convergence when the non-channel regions are included (Figures 4, S1). Instead, the fluvial-marine geomorphic change is ~40-50km inland of the bayhead and seaward of the Mobile-Tensaw bifurcation (~rkm 90-100).

The tide-dominated and river-dominated geometries spatially coincided with their reflective processes when the flood limit was at the geomorphic change. Under these conditions, in the lower delta, the tidal dynamics suggest the reach is *ideal* and in morphodynamic equilibrium, aligning well with geomorphic theory (e.g., Dalrymple & Choi, 2007; Gugliotta & Saito, 2019). However, the hydrodynamic observations show this only occurred at median river discharge conditions (i.e., ~1,000 m^3s^{-1}) as the flood limit shifted longitudinally with river discharge (~±80rkm). Even though a system like the Mobile-Tombigbee fluvial-marine transition may have characteristic geomorphology, the hydrodynamics may be highly variable and difficult to approximate for any given time using only the geometry.

6.2.2 The Height Convergent Backwater

Landward of the sharp geomorphic change is a long backwater reach (i.e., M1; Chow, 1959) with weak height convergence where strong friction damped the tides before amplifying from dam reflection. At low discharge, results suggest the height convergence extended tidal influence inland. Because of the smaller upstream cross-sectional area, a small increase in river discharge quickly attenuated the tide. Kästner et al. (2019) shows this is done directly by increasing friction and indirectly by increasing the water surface slope, reducing convergence. Reduced convergence in the backwater reaches of the Tombigbee River and the Mobile distributary, which was also height convergent, occurred with river discharge increasing the water surface slope while the bed remained stationary (Figure 4b).

Theory indicates the nonlinear interaction of increasing friction while reducing convergence also causes river discharge to 1) increase reflection, which can first

amplifying tides by ~5% before attenuating, and to 2) affect the horizontal tidal component more than the vertical, causing the horizontal tide to attenuate faster and the phase lag to increase and then decrease with river discharge (Kästner et al., 2019). Our results provide observational support for the increased reflection with tidal amplitudes peaking from river discharge (Figure 7) and the higher sensitivity of the horizontal tide to river discharge with the horizontal tide peak amplitude and tidal limit being observed at a lower river discharge and seaward of the vertical tide (Figure 9). The higher sensitivity of the horizontal tide increased the phase lag at low discharge until a higher discharge when the vertical tide also began to strongly respond, which decreased the phase lag, resulting in a phase lag peak (Figure 8).

While height may converge more than width in backwater reaches, a different lateral component can be critical, sinuosity. Sinuosity attenuates tides through flow separation around bends, inducing form friction (Bo & Ralston, 2020), which is not accounted for in analytical tide models (e.g., Kästner et al., 2019; van Rijn, 2012; Buschman et al., 2009). The processes controlling sinuosity remain highly debated (e.g., Schumm & Kahn, 1972; Hoitink et al., 2017, Lazarous & Constintine, 2013). Using planform observations, sinuosity is associated with peaking near the estuarine turbidity maximum, seaward of the flood limit, because of the large sediment availability (e.g., Choi et al., 2020; Leuven et al., 2018). Using planform and depth observations, we show sinuosity increased just landward of the geomorphic change (rkm 96) and coincides with the backwater reach, similar to other systems (e.g., Fly, Yantze, Ganges-Brahmaputra, Irrawaddy; Gugliotta & Saito, 2019). Because backwater reaches have a relatively low availability of medium to coarse grained sediment (Ensign & Noe, 2018; Nittrouer & Viparelli, 2014), sinuosity in the fluvial-marine transition is likely controlled by flow deceleration, as presented theoretically by Lazarous & Constintine (2013). Thus, backwater dynamics that increase height convergence and reduce tidal attenuation also increase sinuosity and form friction, which are two factors that may balance in backwater reaches.

Another complication for backwater analytical theory is dam reflection. Analytical theory using a constant convergence predicts dam reflection amplifies tides and decreases their phase (van Rijn, 2012), as observed in the Ems and Guadalquivir Estuaries (Talke & de Swart, 2006; Díez-Minguito et al., 2012b) and shown here on the Tombigbee River when river discharge was low. Theory indicates the reflected wave becomes negligible beyond half a convergence length (Friedrichs, 2010); suggesting dam effects are minimal seaward of rkm 180. At R194, slow wave celerity across the upper delta suggests the incident and reflected waves were more than a quarter out of phase and reduced the tidal amplitude (Figure 7b). As river discharge increased, the tide attenuated and phase increased, like further seaward (Figure 7), suggesting the tide-river interactions did not greatly change the dam effects. Because the local bed slope is relatively flat (Figure 4b), suggesting the backwater effects were small, a future investigation is warranted for dam effects in reaches with strong backwater effects.

6.2 Broader Applications

The tide-river-geomorphic channel interactions of the Tombigbee-Mobile fluvial-marine transition provides many insights that are broadly applicable. The diurnal microtidal system followed theory developed for semidiurnal and mixed tidal environments with larger tidal ranges. For example, the theories of friction and width convergence are based on the dominant tidal specie and can explain D_2 and the D_4 overtide amplitudes and phases in semidiurnal environments, like the Columbia, Frasier, and St. Lawrence, but not D_1 (Jay & Flinchem, 1997; Godin, 1985). Demonstrating the D_1 tidal amplitude, phase, and wavenumber followed expected theory in a diurnal system provides substantial support for friction being controlled by the dominant tidal specie. This also supports the overtide theory of M2 transferring energy to K1 and O1 to explain the insensitivity of D_1 to river discharge in semidiurnal environments (Godin 1985, 1999). The opposite may also be true in diurnal environments, but this has yet to be observed. The observations presented here may be the first diurnal tide observations to capture tide-river and tide-channel geomorphic interactions, highlighting an unequal portion of studies in semidiurnal systems and a still limited understanding of diurnal environments.

In well-studied semidiurnal systems, observed longitudinal shifts have only been identified to a limited extent, but generally show the distance increases with the relative range of river discharge. In the St. Lawrence, river discharge ranges 0.7 orders of magnitude shifting the flood limit ~38km (7,000-32,000 m^3s^{-1}, Grondines to Deschambault; Matte et al., 2014), in the Yangtze River, modern discharge ranges 0.9 orders of magnitude shifting the flood limit ~85 km (~10,000-80,000 m^3s^{-1}; Zhenjiang to Jiangyin; Guo et al., 2015, Shen, 2003), and in the Columbia River, modern river discharge ranges 1.1 orders of magnitude shifting the flood limit ~110 km (1,800-24,000 m^3s^{-1}; St. Helens to Astoria; Jay et al., 2015; Jay, correspondence). In the diurnal Tombigbee River-Mobile Bay, discharge ranges 2.2 orders of magnitude and the flood limit shifts ~180 km (Figure 9). Following (Eq. 6), for every order of magnitude increase in river discharge, the flood limit and other tide-river interactions shift seaward twice the e-folding length. Because height convergence is reduced by river discharge, the shift may be larger and more complex in these reaches (e.g., backwater), making the tidal limit more difficult to identify than the flood limit.

Flood limits may not exist in all systems and may shift in response to human development. For example, when Q_{rf} is extremely high, like the Mississippi and Amazon Rivers, tidal flows do not reverse, and the flood limit is temporarily seaward of the fluvial-marine transition (Gallo & Vizon, 2005; Hoitink & Jay, 2016). When Q_{rf} is extremely low, like in lagoons and tidal creeks, tidal flows reverse throughout the entire system and no flood limit exists. Both extremes can occur in the same system when rivers are highly regulated. For example, the Guadalquivir River discharge can be completely stopped during draughts, allowing the flood limit to reach the regulating dam. However, for river discharge greater than 3,000 m^3s^{-1} the flood limit is translated 110 km to near the estuary

mouth (Díez-Minguito et al. 2012a; Díez- Minguito, correspondence). Another common human impact is dredging, for shipping channels, which lowers the bed and increases tidal influence while reducing river influence (Ralston et al., 2018). On the Hudson River, the flood limit is often in a region over-deepened by dredging and only shifts ~40km with the typical annual one order of magnitude range in river discharge. However, infrequent, extreme discharge events that are a half an order of magnitude larger can shift the flood limit over ~50km further seaward (Troy to near Tivoli; Ralston & Geyer, 2017; Ralston, correspondence). The smaller inland shift under 'typical flow' conditions is likely a result of an unnaturally large cross-sectional area which now requires a larger river discharge to exceed the tidal discharge and shift the flood limit.

On the other hand, the flood limit location is also a function of tidal energy, which controls the morphodynamic equilibrium of a system. Because tidal energy scales with the damping rate, in a landward direction, tides with more energy attenuate faster (e.g., larger amplitudes, shorter periods; Eq. 3) and should theoretically cause convergence to scale with tidal amplitude. However, empirical investigations have found limited support (e.g., Davies & Woodroffe, 2010; Leuven et al., 2018; Savenije, 2012) and may be a result of grouping all systems regardless of tidal period, which Equation 5 suggests is critical to morphodynamic equilibrium. For example, Savenije (2012) shows area e-folding lengths can range greatly, ~10-100km, but by separating the diurnal and semidiurnal systems, shows that mean area e-folding lengths of the diurnal systems is more than twice the semidiurnal systems. Equation 5 also suggests diurnal systems have longer fluvial-marine transitions (i.e., $T^2 \propto L_p$), reflecting tide-river theory and observations of diurnal tides attenuating landward of semidiurnal tides (e.g., Godin, 1999; Gallo & Vizon, 2005). The longer and less convergent geometries of diurnal systems may also have hydrodynamic feedbacks, suggesting river discharge may cause larger longitudinal shifts in diurnal systems than semidiurnal systems (i.e., Eq. 6).

Like tidal controls on morphodynamics, river discharge shapes the backwater geometry and may also indirectly affect the tide-river longitudinal shifts. High river discharge has a relatively steep water level slope that extends further seaward with resulting currents that scour the bed, creating a deep region at the seaward most location of river dominated geometry (e.g., Figures 1b, 4b). The range of river discharge controls the bed slope and backwater length (Ganti et al., 2019), subsequently increasing height convergence for tides. Thus, not only does a large river event force tide-river interactions far seaward, it also excavates a deep height convergent channel for tides to intrude further landward during low river discharge. These patterns are consistent with proposed river scouring dynamics in the Tombigbee River-Mobile Bay system (Dykstra & Dzwonkowski 2020a), and suggest tide-river longitudinal shifts scale with the range of river discharge due to morphodynamic feedbacks in addition to altering the tidal prism and friction.

6.2.1 Delineating the estuary and tidal river

Dynamic longitudinal shifts do not fit within traditional static definitions of tide-river environments (e.g., *estuary*, Cameron & Prichard, 1963) and require methods that capture their dynamics. The water level method of Hoitink & Jay (2016), capturing the subtidal setup, reliably delineates longitudinal shifts of the estuary-tide river boundary on the Columbia and Hudson Rivers (Jay et al., 2015; Ralston et al., 2017). This method may be preferred to capturing the flood limit with velocity measurements because water level measurements are more common, easier to quality control, and analyze. However, a primary process controlling subtidal setup, Stokes transport, is small in systems with a small tidal amplitude-depth ratio or when highly stratified and can be complicated by tide-river interactions (Jay, 2010; Sassi et al., 2012). All these factors describe our study site and likely explain why the first test of the methodology in a diurnal and microtidal system, shown here (Figure 6a), displayed inconsistent behavior. The method may not be suitable for low energy tidal systems and requires further analysis. The flood limit determined with tidal velocity observations was a more robust estuary-tidal river delineation in this diurnal-mircrotidal system and may be true for other systems. Not only does it reflect a primarily delineation for analytical solutions (e.g., Jay & Flinchem, 1997; van Rijn, 2012; Kästner et al., 2019), it only requires a duration of one tidal cycle per river discharge level and is a general concept that can be more easily communicated to the broader scientific community.

Velocity is also critical for friction and discharge and is commonly converted from water level observations, but this process could produce sizable errors. The conversion assumptions (1: vertical tide represents horizontal tide, 2: tidal wavenumber and phase lag do not change through time, and 3: longitudinal consistency of river discharge, subtidal velocity, and tidal phase lag; Sassi & Hoitink, 2013; Buschman et al., 2009) are appropriate for pristine channels (i.e., constant width and height; Fredericks, 2010; Kästner et al., 2019) but may not be appropriate for realistic environments with convergence and river discharge, like the Tombigbee River-Mobile Bay fluvial-marine transition shown here. Longitudinal complexities of river discharge have been acknowledged in some studies but suggest errors in timing and magnitude should be minimal because river waves are much longer than tidal waves in the fluvial-marine transition, pointing to the long period of river waves (e.g., Jay & Flinchem, 1997; Sassi & Hoitink, 2013). However, the river waves in the delta are slow, and when the system is still impacted by tides, river waves range 350-1,060 km (Dykstra & Dzwonkowski, 2020a). This length is approximately the same as the tidal waves and not much longer than the fluvial-marine transition, indicating river discharge was not spatially consistent. To account for the river wave propagation, river discharge was lagged for each station based on observations of the river waves (Dykstra & Dzwonkowski 2020a), which produced results more consistent with theory. Due to the complexities of tide-river interactions, particularly in backwater environments, simulating horizontal tidal waves from water level observations to

calculate velocity, friction, and discharge may produce sizable errors.

Not only does river discharge affect tides, it can also generates feedbacks that affect the river discharge itself. These feedbacks traditionally show river discharge has a negative feedback by either increasing friction through higher flow, which damps tides and generates subtidal setup, or reducing friction through stratification, which amplifies tides (Jay & Flinchem, 1997, Hoitink & Jay, 2016). This study suggests both processes can occur simultaneously and are interconnected with stratification amplifying tides in an estuary and passing more tidal energy inland, which can cause a larger subtidal setup in the tidal river. Thus, increasing the magnitude of river discharge could generate a larger subtidal setup and reduce the momentum of river discharge, further increasing the negative feedback of river discharge. Positive feedbacks also occur in the backwater reach through river friction increasing river setup and lowering convergence, causing tides to quickly attenuate.

The complex river discharge effects on tides can be summarized as a process modulating the principal channel geomorphic effects on tides: friction and convergence. River discharge reduces friction through stratification, amplifying tides, and increasing friction through river flow interacting with the bed, attenuating tides. River discharge increases height convergence by scouring a sloping bed, amplifying tides, and reduces width convergence with wide channels at the head of a bay or height convergence by increasing the river slope, attenuating tides. Frictional effects can change with each river event, while convergence effects occur naturally over longer geologic timescales. Height convergence in backwater reaches is an exception and can change with each river event, making this region highly dynamic and still poorly understood. Together, the river modulation of friction and convergence in fluvial-marine transitions is spatially variable and can generate large longitudinal shifts of the tidal river and estuary, as demonstrated and analytically described in this study.

7 Conclusions

Tide-river-geomorphic interactions are studied in the diurnal microtidal Tombigbee River-Mobile Bay fluvial-marine transition with water level, velocity, and discharge observations, where the large range in river discharge made the system highly dynamic. From this study, the findings include:

1. Longitudinal shifts in tide-river interactions (e.g., flood limit, tidal limit) are primarily controlled by the ratio of river discharge to tidal discharge and convergence, which, as river discharge fluctuated, shifted the flood and tidal limits ~180km.

2. River discharge simultaneously amplified tides in seaward reaches while damping tides in landward reaches, passing more tidal energy inland where it attenuated faster and may have generated feedbacks.

3. Diurnal tides amplified from convergence and attenuated where convergence was small, supporting theory that tidally generated friction is created by the dominant tidal species; either diurnal or semidiurnal.

4. Analyses of the geometry revealed a width convergent seaward reach and height convergent and sinuous landward reach in a microtidal diurnal system, suggesting the established geomorphic transition is broadly applicable. Analytical equations suggest tidal characteristics affect the transition length scales, making diurnal systems less convergent, longer, and subsequently more sensitive to river discharge effects (Eq. 5).

5. In backwater reaches, river discharge events reduced height convergence and increased friction, making tidal currents attenuate faster and become more delayed with river discharge than tidal observations using water level.

We provide reduced complexity analytical solutions for estimating the shifting locations of the flood limit and river attenuation of tides (Eq. 6) as well as tidal effects on system geometry (Eq. 5). Understanding these tide-river-geomorphic interactions are important now (e.g., sediment/nutrient transport, navigation, recreation) and in the future, as communities develop new infrastructure, insurance plans, and manage natural resources under the pressures of global warming, sea level rise, and altered river flows.

Acknowledgments, Samples, and Data

This research was funded through the Dauphin Island Sea Lab-Food and Drug Administration Fellowship, the NOAA RESTORE Science Program (NA17NOS4510101, NA19NOS4510194), the University of South Carolina Advanced Support Program for Innovative Research Excellence-II, and a NASA SC EPSCoR Award (NNX16AR02A). We would like to thank K. Calci, K. Dorgan, B. Webb, and A. Valle-Levinson for their advice and encouragement, as well as the correspondence with M. Díez-Minguito, D. Ralston, D. Jay, P. Matte, and S. Talke. We are unaware of any perceived financial conflicts of interests or affiliations. All data needed to recreate this analysis are publicly available through sources mentioned in the main text and Table S1 of the Supplementary Information.

References

Bo, T., and D. K. Ralston (2020), Flow Separation and Increased Drag Coefficient in Estuarine Channels With Curvature, *J. Geophys. Res. Oceans*, *125*(10), W02402–25. https://10.1029/2020JC016267

Burchard, H., H. M. Schuttelaars, and D. K. Ralston (2018), Sediment Trapping in Estuaries, *Annu. Rev. Marine. Sci.*, *10*(1), 371–395. https://10.1146/annurev-marine-010816-060535

Buschman, F. A., A. J. F. T. Hoitink, M. van der Vegt, and P. Hoekstra (2009), Subtidal water level variation controlled by river flow and tides, *Water Resour. Res.*, *45*(10), 7715–12. https://10.1029/2009WR008167

Byrnes, M. R., S. F. Griffee, and M. S. Osler (2010), *Channel Dredging and Geomorphic Response at and Adjacent to Mobile Pass, Alabama*, US Army Corps of Engineers.

Cai, H., H. H. G. Savenije, and M. Toffolon (2014), Linking the river to the estuary: influence of river discharge on tidal damping, *Hydrol. Earth Syst. Sci.*, *18*(1), 287–304. https://10.5194/hess-18-287-2014

Cameron, W.M., Pritchard, D.W. (1963) Estuaries, in *The Sea*, New York: Wiley Interscience Publ., vol. 2, pp. 306–324.

Cartwright, D. E. (1971). Tides and waves in the vicinity of Saint Helena. Philosophical Transactions of the Royal Society of London A: Mathematical, Physical and Engineering Sciences, 270(1210), 603–646. https://doi.org/10.1098/rsta.1971.0091

Choi, K., D. Kim, and J. Jo (2020), Morphodynamic evolution of the macrotidal Sittaung River estuary, Myanmar: Tidal versus seasonal controls, *Marine Geology*, *430*, 106367. https://10.1016/j.margeo.2020.106367

Chow, T. V. (1959). Open-channel hydraulics (Vol. 1). New York: McGraw-Hill.

Dalrymple, R. W., and K. Choi (2007), Morphologic and facies trends through the fluvial–marine transition in tide-dominated depositional systems: A schematic framework for environmental and sequence-stratigraphic interpretation, *Earth-Science Reviews*, *81*(3-4), 135–174. https://10.1016/j.earscirev.2006.10.002

Dalrymple, R. W., C. E. Kurcinka, and B. V. Jablonski (2015), Deciphering the relative importance of fluvial and tidal processes in the fluvial–marine transition, *Elsevier*. https://10.1016/B978-0-444-63529-7.00002-X

Davis Jr, R. A. 2011. Tidal signatures and their preservation potential in stratigraphic sequences. In *Principles of tidal sedimentology*, ed. R. A. Davis Jr & R. W. Dalrymple, pp. 35–55, Springer Science & Business Media.

Davies, G., & Woodroffe, C. D. (2010). Tidal estuary width convergence: Theory and form in North Australian estuaries. *Earth Surface Processes and Landforms*, *35*(7), 737–749. https://doi.org/10.1002/esp.1864

Díez-Minguito, M., Baquerizo, A., Ortega-Sanchez, M., Navarro, G., & Losada, M. A. (2012). Tide transformation in the Guadalquivir estuary (SW Spain) and process-based zonation. *Journal of Geophysical Research*, *117*(C3), 1–14. https://doi.org/10.1029/2011jc007344

Díez-Minguito, M., A. Baquerizo, M. Ortega-Sanchez, I. Ruiz, and M. A. Losada (2012b), Tidal wave reflection from the closure dam in the Guadalquivir Estuary (SW Spain), *Coastal Engineering*, 1–8.

Dronkers, J. (2017), Convergence of estuarine channels, *Continental Shelf Research*, *144*, 120–133. https://10.1016/j.csr.2017.06.012

Dykstra, S. L., and B. Dzwonkowski (2020a), The propagation of fluvial flood waves through a backwater-estuarine environment, *Water Resour. Res.*, *56*(2), e25743. https://10.1029/2019WR025743

Dykstra, S. L.; Dzwonkowski, B. (2020b). The Thalweg and Sub-Tidal Flow of a Backwater-Estuarine Environment, Alabama; Gulf of Mexico Research Initiative Information & Data Cooperative Consortium for Oil Spill Exposure Pathways in Coastal River-Dominated Ecosystems. https://doi.org/10.7266/6TDW4XSV

Dykstra, S. L.; Dzwonkowski, B. (in review). Intensifying precipitation increases the frequency of coastal river flooding and compound fluvial-marine events. *Water Resources Research*.

Dzwonkowski, B., K. Park, and R. Collini (2015), The coupled estuarine-shelf response of a river-dominated system during the transition from low to high discharge, *J. Geophys. Res. Oceans*, *120*(9), 6145–6163. https://10.1002/2015JC010714

Dzwonkowski, B., S. Fournier, J. T. Reager, S. Milroy, K. Park, A. M. Shiller, A. T. Greer, I. Soto, S. L. Dykstra, and V. Sanial (2018), Tracking sea surface salinity and dissolved oxygen on a river-influenced, seasonally stratified shelf, Mississippi Bight, northern Gulf of Mexico, *Continental Shelf Research*, *169*, 25–33. https://10.1016/j.csr.2018.09.009

Ensign, S. H., and G. B. Noe (2018), Tidal extension and sea-level rise: recommendations for a research agenda, *Front Ecol Environ*, *16*(1), 37–43. https://10.1002/fee.1745

Farr, T.G., Rosen, P.A., Caro, E., Crippen, R., Duren, R., Hensley, S., Kobrick, M., Paller, M., Rodriguez, E., Roth, L., Seal, D., Shaffer, S., Shimada, J., Umland, J., Werner, M., Oskin, M., Burbank, D., Alsdorf, D. (2007), The Shuttle Radar Topography Mission, Rev. Geophys., 45, RG2004. https://doi.org/10.1029/2005RG000183

Friedrichs, C. T., and D. G. Aubrey (1994), Tidal propagation in strongly convergent channels, *J. Geophys. Res.*

Friedrichs, C. T. (2010), Barotropic tides in channelized estuaries. In *Contemporary Issues in Estuarine Physics*, ed. A Valle-Levinson, pp. 12–26. Cambridge, UK: Cambridge Univ. Press.

Gallo, M. N., and S. B. Vinzon (2005), Generation of overtides and compound tides in Amazon estuary, *Ocean Dynamics*, *55*(5-6), 441–448. https://10.1007/s10236-005-0003-8

Ganti, V., M. P. Lamb, and A. J. Chadwick (2019), Autogenic Erosional Surfaces in Fluvio-deltaic Stratigraphy from Floods, Avulsions, and Back-

water Hydrodynamics, *Journal of Sedimentary Research*, *89*(8), 815–832. https://10.2110/jsr.2019.40

Godin, G. (1985). Modification of River Tides by the Discharge. *Journal of Waterway, Port, Coastal, and Ocean Engineering*, *111*(2), 257–274. https://doi.org/10.1061/(asce)0733-950x(1985)111:2(257)

Godin, G. (1999). The Propagation of Tides up Rivers With Special Considerations on the Upper Saint Lawrence River. *Estuarine, Coastal and Shelf Science*, *48*(3), 307–324. https://doi.org/10.1006/ecss.1998.0422

Green, J. A. M. (2010), Ocean tides and resonance, *Ocean Dynamics*, *60*(5), 1243–1253. https://10.1007/s10236-010-0331-1

Greene, D. L., Jr, A. B. Rodriguez, and J. B. Anderson (2007), Seaward-Branching Coastal-Plain and Piedmont Incised-Valley Systems Through Multiple Sea-Level Cycles: Late Quaternary Examples from Mobile Bay and Mississippi Sound, U.S.A, *Journal of Sedimentary Research*, *77*(2), 139–158. https://10.2110/jsr.2007.016

Greer, A. T. et al. (2018), Functioning of Coastal River-Dominated Ecosystems and Implications for Oil Spill Response: From Observations to Mechanisms and Models, *Oceanography*, *31*(3). https://10.5670/oceanog.2018.302

Grinsted, A., J. C. Moore, and S. Jevrejeva (2004), Application of the cross wavelet transform and wavelet coherence to geophysical time series, *Nonlinear Processes in Geophysics*, *11*(5), 561–566. https://10.5194/npg-11-561-2004

Gunter, G., Ballard, B. S., & Venkataramiah, A. (1974). A review of salinity problems of organisms in United States coastal areas subject to the effects of engineering works. *Gulf and Caribbean Research*, *4*(3), 380-475.

Gugliotta, M., and Y. Saito (2019), Matching trends in channel width, sinuosity, and depth along the fluvial to marine transition zone of tide-dominated river deltas: The need for a revision of depositional and hydraulic models, *Earth-Science Reviews*, *191*, 93–113. https://10.1016/j.earscirev.2019.02.002

Guo, L., M. van der Wegen, D. A. Jay, P. Matte, Z. B. Wang, D. Roelvink, and Q. He (2015), River-tide dynamics: Exploration of nonstationary and nonlinear tidal behavior in the Yangtze River estuary, *J. Geophys. Res. Oceans*, *120*(5), 3499–3521. https://10.1002/2014JC010491

Ha, H. K., & Park, K. (2012). High-resolution comparison of sediment dynamics under different forcing conditions in the bottom boundary layer of a shallow, micro-tidal estuary. *Journal of Geophysical Research*, *117*(C6), n/a-n/a. https://doi.org/10.1029/2012jc007878

Haigh, I. D. et al. (2020), The Tides They Are A-Changin': A Comprehensive Review of Past and Future Nonastronomical Changes in Tides, Their Driving Mechanisms, and Future Implications, *Reviews of Geophysics*, *58*(1), 1–39. https://10.1029/2018RG000636

Hoitink, A. J. F. T., and D. A. Jay (2016), Tidal river dynamics: implications for deltas, *Reviews of Geophysics*. https://10.1002/(ISSN)1944-9208

Hoitink, A. J. F. T., Z. B. Wang, B. Vermeulen, Y. Huismans, and K. Kästner (2017), Tidal controls on river delta morphology, *Nature Geosci*, *10*(9), 637–645. https://10.1038/ngeo3000

Horrevoets, A. C., Savenije, H. H. G., Schuurman, J. N., & Graas, S. (2004). The influence of river discharge on tidal damping in alluvial estuaries. *Journal of Hydrology*, *294*(4), 213–228. https://doi.org/10.1016/j.jhydrol.2004.02.012

Jay, D. A. (1991), Green's law revisited: Tidal long-wave propagation in channels with strong topography, *J. Geophys. Res. Oceans*, *96*(C11), 20585–20598. https://10.1029/91JC01633.

Jay, D. A. (2010), Estuarine variability. In *Contemporary Issues in Estuarine Physics*, ed. A Valle-Levinson, pp. 12–26. Cambridge, UK: Cambridge Univ. Press

Jay, D. A., and E. P. Flinchem (1997), Interaction of fluctuating river flow with a barotropic tide: A demonstration of wavelet tidal analysis methods, *J. Geophys. Res.* https://10.1029/96JC00496/full.

Jay, D. A., K. Leffler, H. L. Diefenderfer, and A. B. Borde (2015), Tidal-fluvial and estuarine processes in the lower Columbia River: I. Along-channel water level variations, Pacific Ocean to Bonneville Dam, *Estuaries and Coasts*. https://10.1007/s12237-014-9819-0.

Kästner, K., A. J. F. T. Hoitink, B. Vermeulen, T. J. Geertsema, and N. S. Ningsih (2017), Distributary channels in the fluvial to tidal transition zone, *Journal of Geophysical Research: Earth Surface*, *122*(3), 696–710. https://10.1002/2016JF004075

Kästner, K., A. J. F. T. Hoitink, P. J. J. F. Torfs, E. Deleersnijder, and N. S. Ningsih (2019), Propagation of tides along a river with a sloping bed, *J. Fluid Mech.*, *872*, 39–73. https://10.1017/jfm.2019.331

Kim, C.-K., and K. Park (2012), A modeling study of water and salt exchange for a micro-tidal, stratified northern Gulf of Mexico estuary, *Journal of Marine Systems*, *96-97*(C), 103–115. https://10.1016/j.jmarsys.2012.02.008

Lane, E. W. (1957). A study of the shape of channels formed by natural streams flowing in erodible material, United States Army Corps of Engineers.

Lazarus, E. D., & Constantine, J. A. (2013). Generic theory for channel sinuosity (Vol. 110, pp. 8447–8452). Proceedings of the National Academy of Sciences. https://doi.org/10.1073/pnas.1214074110

Leuven, J. R. F. W., B. van Maanen, B. R. Lexmond, B. V. van der Hoek, M. J. Spruijt, and M. G. Kleinhans (2018), Dimensions of fluvial-tidal meanders: Are they disproportionally large? *Geol*, 1–4. https://10.1130/G45144.1

Leopold, L. B., M. G. Wolman, and J. P. Miller (1964), Fluvial Processes in Geomorphology, W. H. Freeman, New York.

Losada, M. A., M. Díez-Minguito, and M. Á. Reyes-Merlo (2017), Tidal-fluvial interaction in the Guadalquivir River Estuary: Spatial and frequency-dependent response of currents and water levels, *J. Geophys. Res. Oceans*, *122*(2), 847–865. https://10.1002/2016JC011984

Matte, P., Y. Secretan, and J. Morin (2014), Temporal and spatial variability of tidal-fluvial dynamics in the St. Lawrence fluvial estuary: An application of nonstationary tidal harmonic analysis, *J. Geophys. Res. Oceans*, *119*(9), 5724–5744. https://10.1002/2014JC009791

McLachlan, R., A. Ogston, and M. A. Allison (2017), Implications of tidally-varying bed stress and intermittent estuarine stratification on fine-sediment dynamics through the Mekong's tidal river to estuarine reach, *Continental Shelf Research*, *147*, 27–37. https://10.1016/j.csr.2017.07.014

Myrick, R. M., & Leopold, L. B. (1963). *Hydraulic geometry of a small tidal estuary.* United States Geological Survey.

Nittrouer, J., Viparelli, E (2014), Sand as a stable and sustainable resource for nourishing the Mississippi River delta. Nature Geosci 7, 350–354. https://10.1038/ngeo2142

NOAA National Geophysical Data Center (2009), Mobile, Alabama 1/3 arc-second NAVD 88 Coastal Digital Elevation Model, NOAA National Centers for Environmental Information, Accessed 2016.

Noble, M. A., W. W. Schroeder, W. J. Wiseman Jr., H. F. Ryan, and G. Gelfenbaum (1996), Subtidal circulation patterns in a shallow, highly stratified estuary: Mobile Bay, Alabama, *J. Geophys. Res.* https://10.1029/96JC02506/full

Nunes, R., & Lennon, G. (1986). Physical property distributions and seasonal trends in Spencer Gulf, South Australia: an inverse estuary. *Marine and Freshwater Research*, *37*(1), 39–53. https://doi.org/10.1071/mf9860039

Pawlowicz, R., B. Beardsley, and S. J. Lentz (2002), Classical tidal harmonic analysis including error estimates in MATLAB using T_TIDE, *Computers & Geosciences*, *28*(8), 929–937. https://10.1016/S0098-3004(02)00013-4

Phillips, C. B., and D. J. Jerolmack (2016), Self-organization of river channels as a critical filter on climate signals, *Science*, *352*(6), 694–697. https://10.1126/science.aad3348

Ralston, D. K., and W. R. Geyer (2017), Sediment Transport Time Scales and Trapping Efficiency in a Tidal River, *Journal of Geophysical Research: Earth Surface*, *122*(11), 2042–2063. https://10.1002/2017JF004337

Ralston, D. K., and W. R. Geyer (2019), Response to Channel Deepening of the Salinity Intrusion, Estuarine Circulation, and Stratification in an Urbanized Estuary, *J. Geophys. Res. Oceans*, *23*, 86–19. https://10.1029/2019JC015006

Ralston, D. K., S. A. Talke, W. R. Geyer, H. Al'Zubadaei, and C. K. Sommerfield (2018), Bigger tides, less flooding: Effects of dredging on barotropic dynamics in a highly modified estuary, *J. Geophys. Res. Oceans*, 2018JC014313–16. https://10.1029/2018JC014313

Robinson, W. H., and W. J. Powell (1956), *Water resources of the Mobile area, Alabama*, United States Department of the Interior.

Rossi, V. M., S. G. Longhitano, D. Mellere, R. W. Dalrymple, R. J. Steel, D. Chiarella, and C. Olariu (2017), Interplay of tidal and fluvial processes in an early Pleistocene, delta-fed, strait margin (Calabria, Southern Italy), *Marine and Petroleum Geology*, 1–17. https://10.1016/j.marpetgeo.2017.02.021

Ruhl, C. A., and M. R. Simpson (2005), *Computation of discharge using the index-velocity method in tidally affected areas*, United States Geological Society.

Sassi, M. G., A. J. F. T. Hoitink, B. de Brye, and E. Deleersnijder (2012), Downstream hydraulic geometry of a tidally influenced river delta, *J. Geophys. Res.*, *117*(F4), 1–13. https://10.1029/2012JF002448

Sassi, M. G., and A. J. F. T. Hoitink (2013), River flow controls on tides and tide-mean water level profiles in a tidal freshwater river, *J. Geophys. Res. Oceans*, *118*(9), 4139–4151. https://10.1002/jgrc.20297

Savenije, H. H. G. (2012). *Salinity and Tides in Alluvial Estuaries, completely revised 2nd edition* (2nd ed.). Delft, The Netherlands: University of Delft.

Schumm, S. A., & Khan, H. R. (1972). Experimental Study of Channel Patterns. *Geological Society of America Bulletin*, *83*(6), 1755. https://doi.org/10.1130/0016-7606(1972)83[1755:esocp]2.0.co;

Schroeder, W. W., Dinnel, S. P., & Jr., W. J. W. (1990). Salinity stratification in a river-dominated estuary. *Estuaries*, *13*(2), 145. https://doi.org/10.2307/1351583

Seim, H. E., Kjerfve, B., & Sneed, J. E. (1987). Tides of Mississippi Sound and the Adjacent Continental Shelf. *Estuarine, Coastal and Shelf Science*. https://doi.org/https://doi.org/10.1016/0272-7714(87)90118-1

Shen, H. T. (Ed.) (2003), Saltwater Intrusion in the Changjiang Estuary [in Chinese], China Ocean Press, Beijing.

Sisulak, C. F., and S. E. Dashtgard (2012), Seasonal Controls On the Development And Character of Inclined Heterolithic Stratification In A Tide-Influenced, Fluvially Dominated Channel: Fraser River, Canada, *Journal of Sedimentary Research*, *82*(4), 244–257. https://10.2110/jsr.2012.21

Smith, W. E. (1997). *A Field Guide to Mobile Delta Geomorphology*. Tuscaloosa, AL: Geological Society of Alabama.

Sulaiman, Z. A., Viparelli, E., Torres, R., Yankovsky, A., & Grego, J. (2021). The Influence of Tides on Coastal Plain Channel Geomorphology: Altamaha

River, Georgia, USA. *Journal of Geophysical Research: Earth Surface*, *126*(7). https://doi.org/10.1029/2020jf005839

Talke, S. A., and D. A. Jay (2020), Changing Tides: The Role of Natural and Anthropogenic Factors, *Annu. Rev. Marine. Sci.*, *12*(1), annurev–marine–010419–010727–31. https://10.1146/annurev-marine-010419-010727

Talke, S. A., and H. E. de Swart (2006), *Hydrodynamics and Morphology in the Ems/Dollard Estuary: Review of Models, Measurements, Scientific Literature, and the Effects of Changing Conditions*, University of Utrecht.

Talke, S. A., H. E. de Swart, and H. M. Schuttelaars (2009), Feedback between residual circulations and sediment distribution in highly turbid estuaries: An analytical model, *Continental Shelf Research*, *29*(1), 119–135. https://10.1016/j.csr.2007.09.002

USGS (2016). 3D Elevation Program (3DEP) Lidar, USGS LPC AL MobileCo 2014 LAS 2016. distributed by OpenTopography. https://portal.opentopography.org

USGS (2020). 3D Elevation Program (3DEP) Lidar, USGS LPC AL 25Co B8 2017. distributed by OpenTopography. https://portal.opentopography.org

Valle-Levinson, A., C. A. F. Schettini, and E. C. Truccolo (2019), Subtidal variability of exchange flows produced by river pulses, wind stress and fortnightly tides in a subtropical stratified estuary, *Estuarine, Coastal and Shelf Science*, *221*, 72–82. https://10.1016/j.ecss.2019.03.022

van den Berg, J. H., and Boersma, J. R. (2007). Diagnostic sedimentary structures of the fluvial-tidal transition zone–Evidence from deposits of the Rhine and Meuse. *Netherlands Journal of Geosciences*.

van Rijn, L. C. (2011), Analytical and numerical analysis of tides and salinities in estuaries; part I: tidal wave propagation in convergent estuaries, *Ocean Dynamics*, *61*(11), 1719–1741. https://10.1007/s10236-011-0453-0

Waselkov, G. A., C. F. Andrus, and G. E. Plumb (Eds.) (2016), *A State of Knowledge of the Natural, Cultural, and Economic Resources of the Greater Mobile-Tensaw River Area*, U.S. Department of the Interior.

Webb, B. M., and C. Marr (2016), Spatial Variability of Hydrodynamic Timescales in a Broad and Shallow Estuary: Mobile Bay, Alabama, *Journal of Coastal Research*, *32*(6), 1374–1388. https://10.2112/JCOASTRES-D-15-00181.1

Winterwerp, J. C., and Z. B. Wang (2013), Man-induced regime shifts in small estuaries—I: theory, *Ocean Dynamics*, *63*(11-12), 1279–1292. https://10.1007/s10236-013-0662-9

Wright, L. D., Coleman, J. M., & Thom, B. G. (1973). Processes of Channel Development in a High-Tide-Range Environment: Cambridge Gulf-Ord River Delta, Western Australia. *The Journal of Geology*, *81*(1), 15–41. https://doi.org/10.1086/627805

Yankovsky, A. E., R. Torres, L. M. Torres-Garcia, and K. Jeon (2012), Interaction of Tidal and Fluvial Processes in the Transition Zone of the Santee River, SC, USA, *Estuaries and Coasts*, *35*(6), 1500–1509. https://10.1007/s12237-012-9535-6

Zhou, Z., G. Coco, M. Jiménez, M. Olabarrieta, M. van der Wegen, and I. Townend (2014), Morphodynamics of river-influenced back-barrier tidal basins: The role of landscape and hydrodynamic settings, *Water Resour. Res.*, *50*(12), 9514–9535. https://10.1002/2014WR015891

Figures

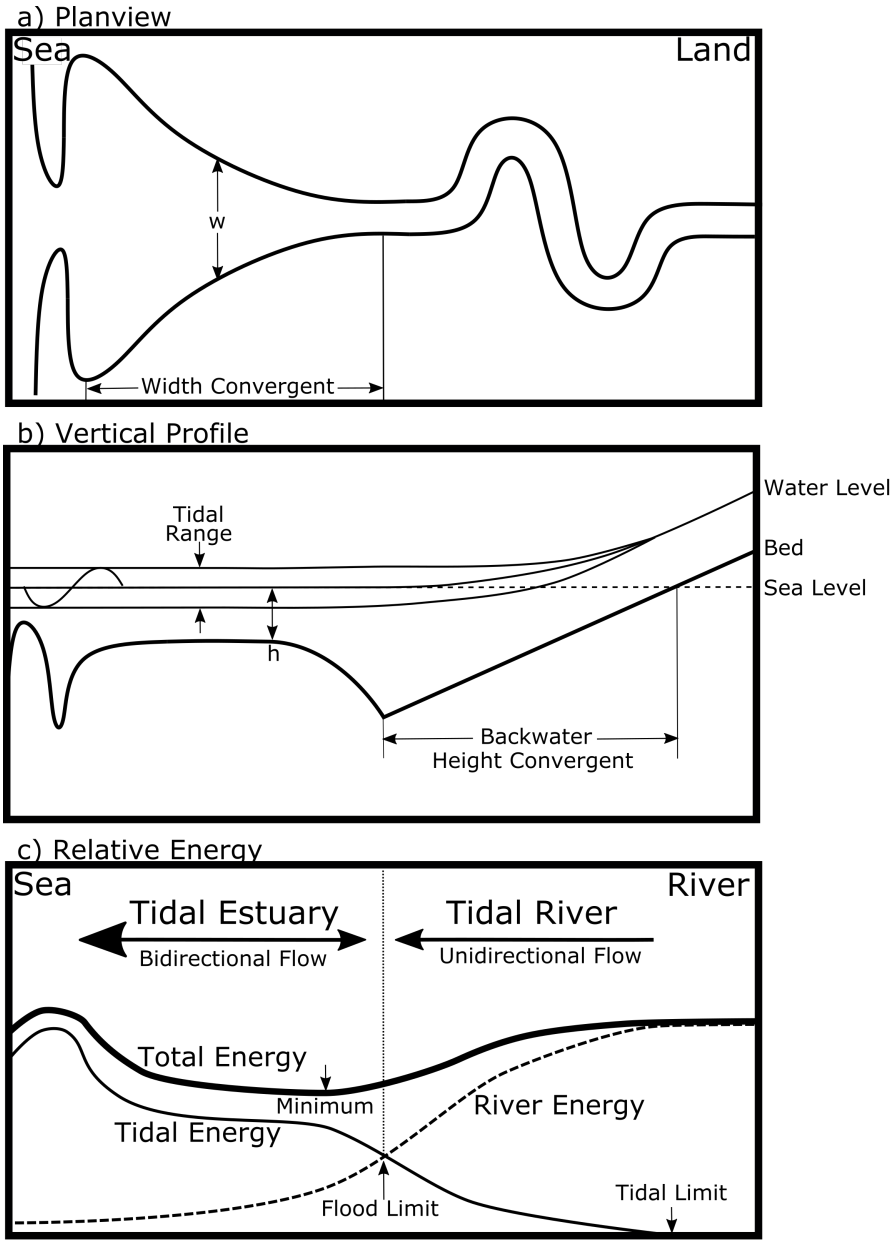

Figure 1. Cartoon of a fluvial-marine transition, showing the a) planview, b) vertical profile, and c) relative river and tidal energy. (Modified from Dalrymple & Choi 2007)

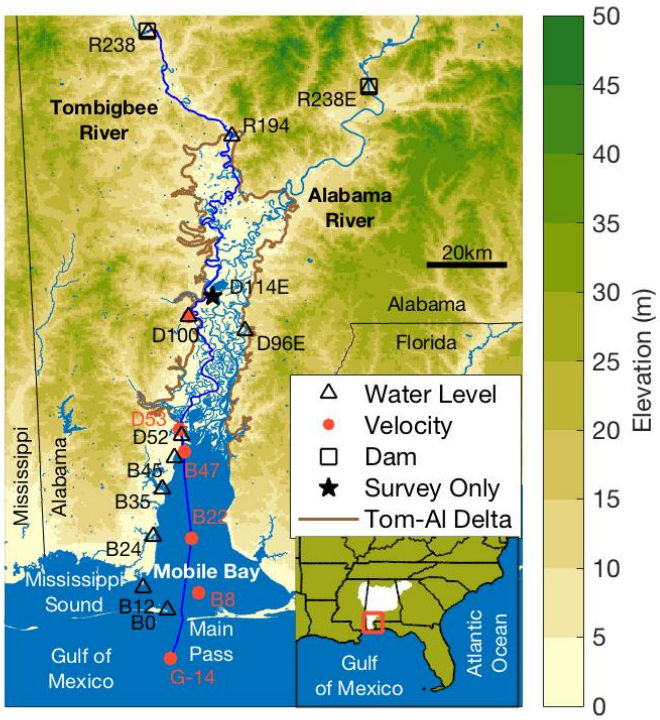

Figure 2. A map of the coastal region of Alabama showing the location of the long-term stations. The longitudinal transect along the Gulf of Mexico, Mobile Bay, Mobile Distributary, and Tombigbee River is shown with a dark blue line.

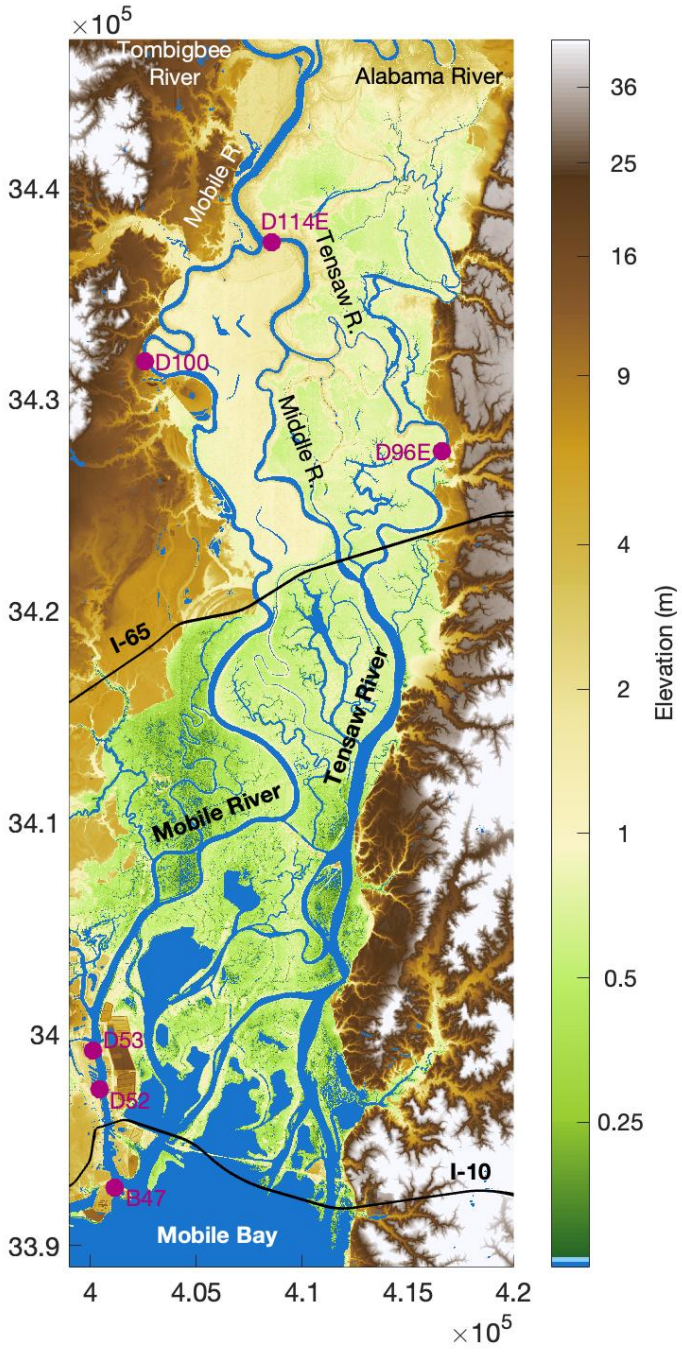
×10^5
Tombigbee River
Alabama River
Mobile R.
D114E
Tensaw R.
D100
Middle R.
D96E
I-65
Tensaw River
Mobile River
D53
D52
B47
I-10
Mobile Bay
34.4
34.3
34.2
34.1
34
33.9
4
4.05
4.1
4.15
4.2
×10^5
36
25
16
9
4
2
1
0.5
0.25
Elevation (m)

Figure 3. A map of the middle and lower Tombigbee-Alabama Delta from the Tombigbee-Alabama confluence to Mobile Bay. Axes units are in meters for UTM zone 16R.

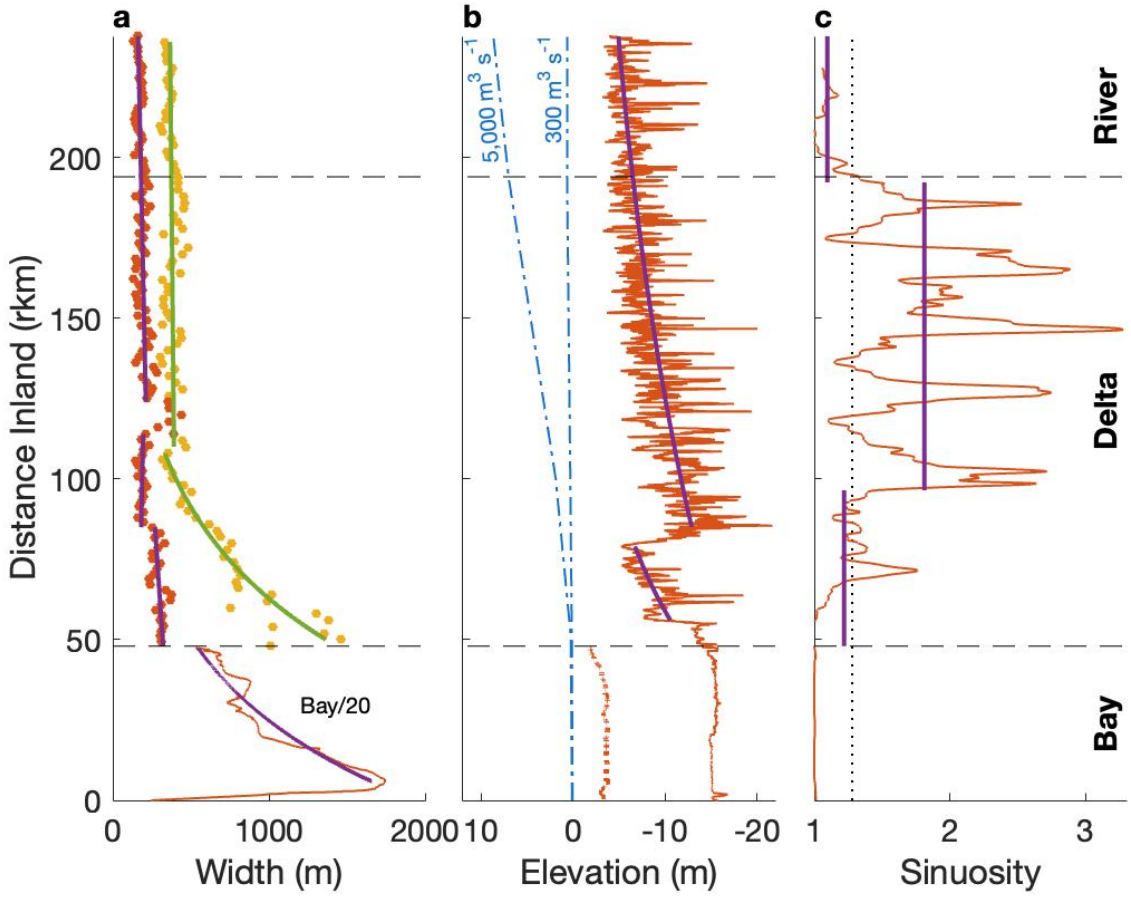

Figure 4. Geometry of the fluvial-marine transition, including a) width, b) depth, and c) sinuosity. The longitudinal transect of Mobile Bay-Mobile River-Tombigbee River (see Fig. 2) is red and log fit with purple lines. Horizontal dashed lines (black) delineate the bay, delta, and non-deltaic rivers. a) In addition to the longitudinal width, the width of the Tensaw Distributary (including the Middle River) and Alabama River is added to capture a summed channel width (yellow dots, green line). To fit the wide bay, the bay width is divided by 20. b) Depth is shown using thalweg elevation (NAVD88) and water levels (dot-dash blue lines) for mean low-flow (~300 m^3s^{-1}) and near bankfull conditions (~5,000 m^3s^{-1}). Thalweg elevations along the bay capture the dredged shipping channel, which is much deeper than the overall mean bay elevation (dotted red line). c) Sinuosity is delineated as being negligible below ~1.28 (dotted line;

Lazarus & Constantine 2013).

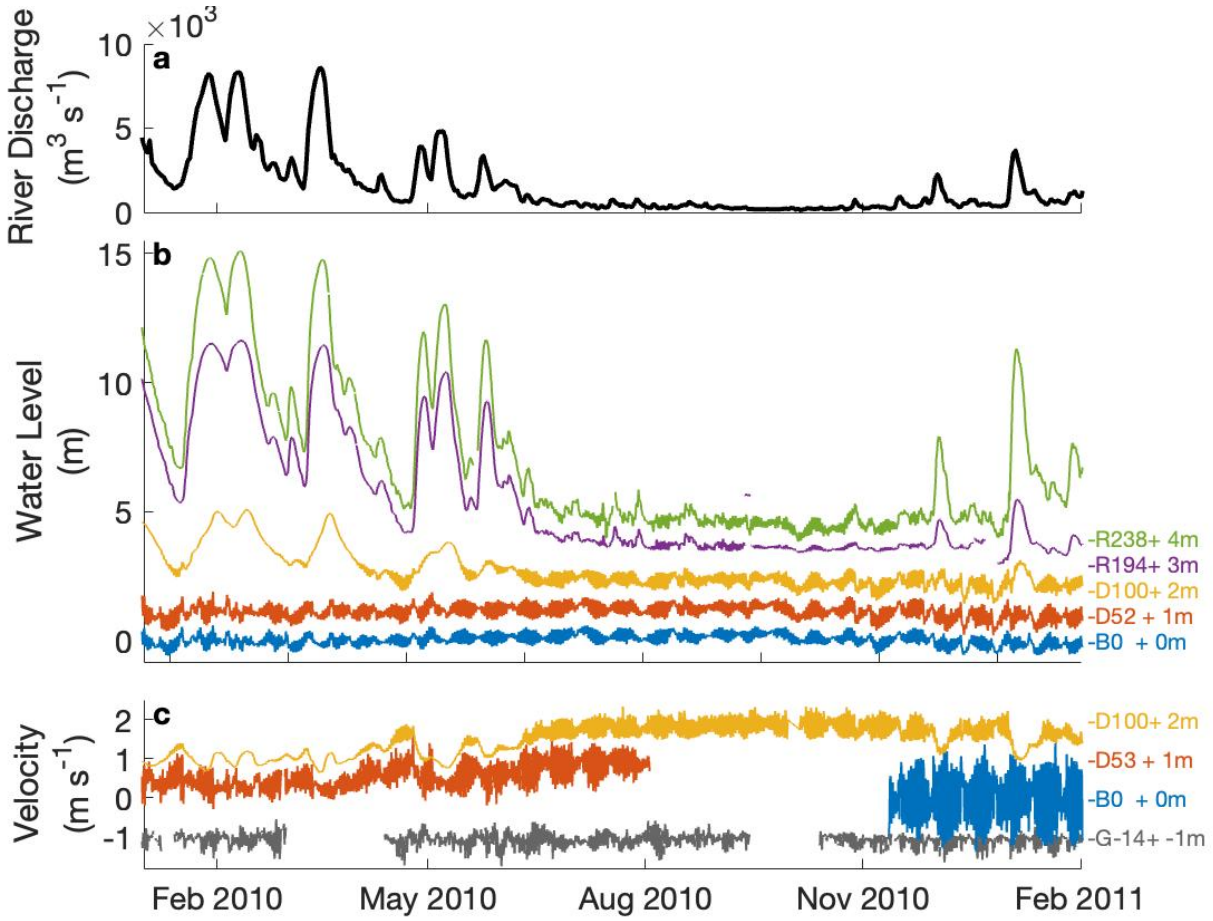

Figure 5. Time series of (a) discharge, (b) water level, and (c) near surface velocity in 2010 showing tidal variability throughout the Alabama coastal region (Fig. 2). For b and c, the measurements at each station are spaced by one unit and labeled on the right. Neighboring stations or coupled instrumentation have the same color.

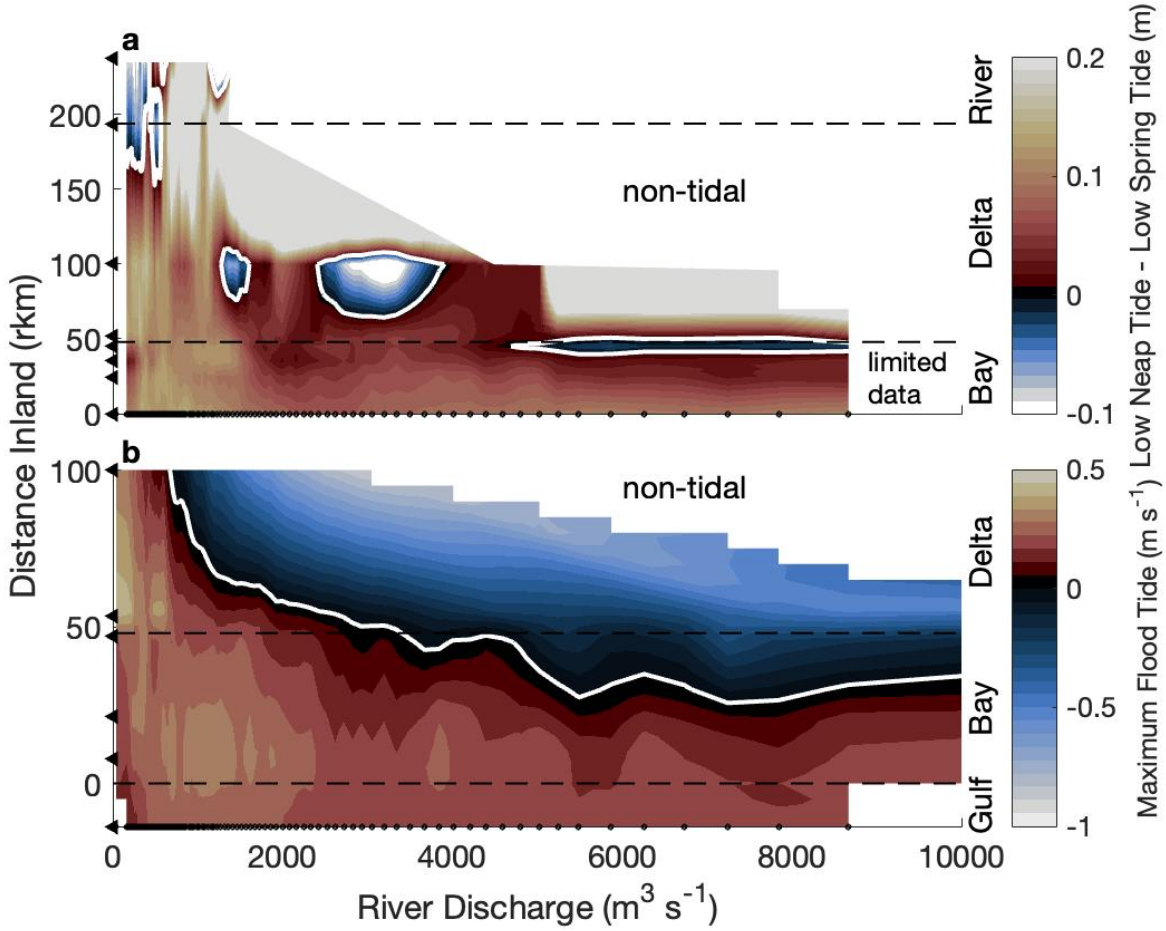

Figure 6. The estuary-tidal river boundary is delineated by discharge conditions using a) the difference between lowest neap water levels and lowest spring water levels (e.g., Hoitink & Jay 2016) and b) the maximum tidal velocity produced by the flood tide. Positive (seaward flow) values suggest estuarine conditions (red/yellow), negative values suggest tidal river conditions (blue), and the delineated boundary is a white line. The y-axis of each subplot shows station locations (triangles) and has different scales, while the x-axis shows bin spacing of river discharge levels (dots, n=101). The white space is either non-tidal or had insufficient data for the analysis.

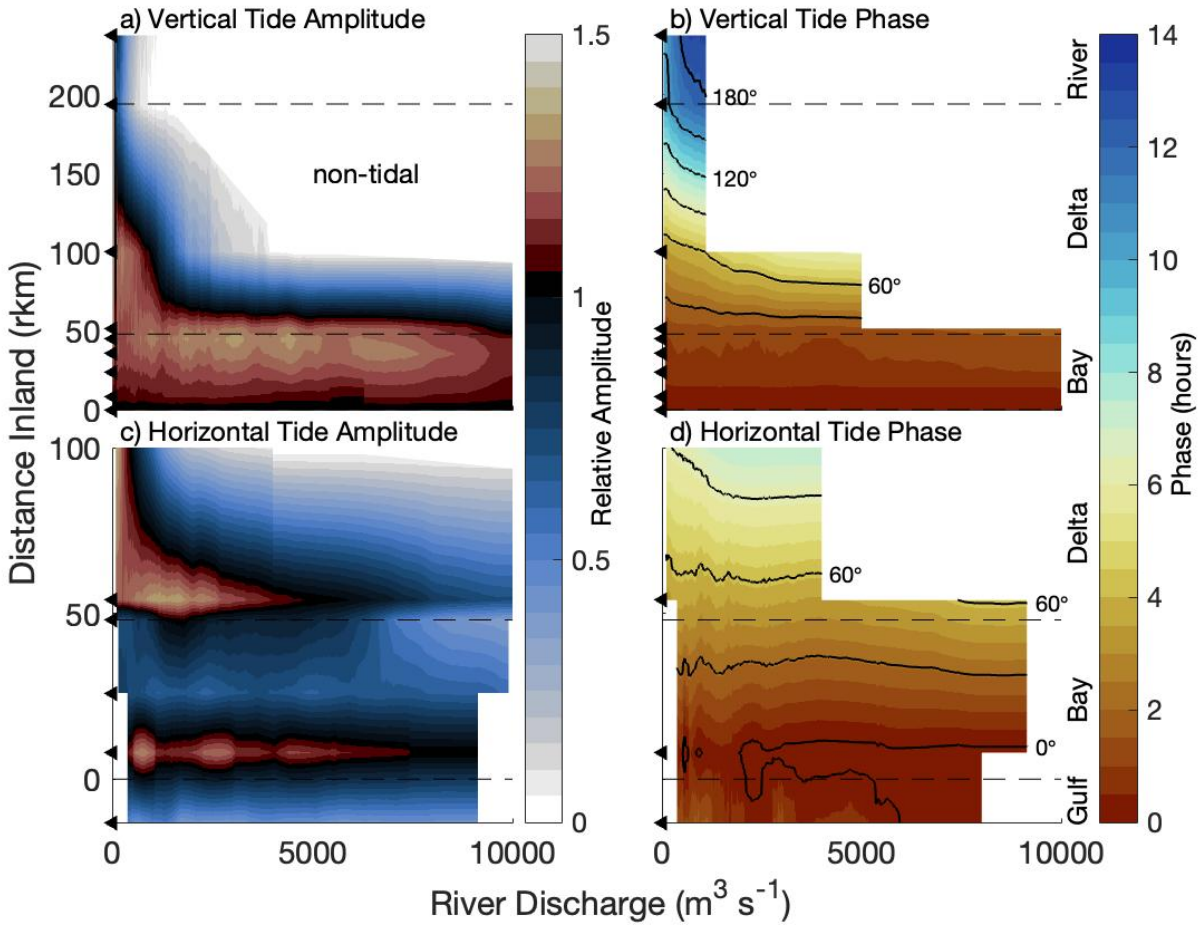

Figure 7. Diurnal tide observations in longitude-river discharge space of the tidal (a,c) amplitude and (b,d) phase of (a,b) the vertical tide observed using water levels and (c,d) the horizontal tide observed using near surface velocity. Amplitudes and phases are normalized to the estuary mouth to show changes longitudinally. The layout of each subplot follows Figure 6.

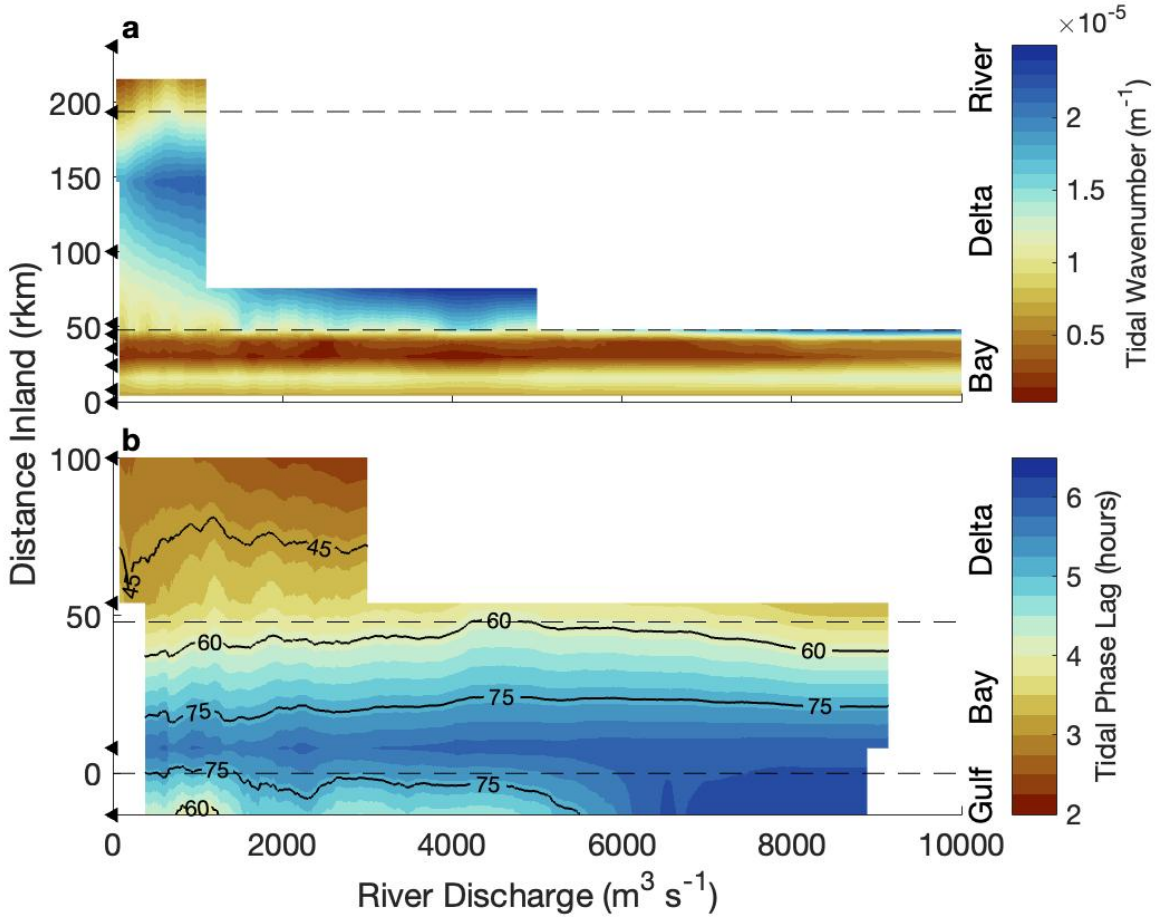

Figure 8. The propagation of diurnal tidal waves is captured using (a) wavenumber and (b) phase lag ($D1_\phi$) in longitude-river discharge space. (b) Black contours show degrees. The layout of each subplot follows Figure 6, except for the wavenumber values in (a), which were resolved at the midpoint between stations.

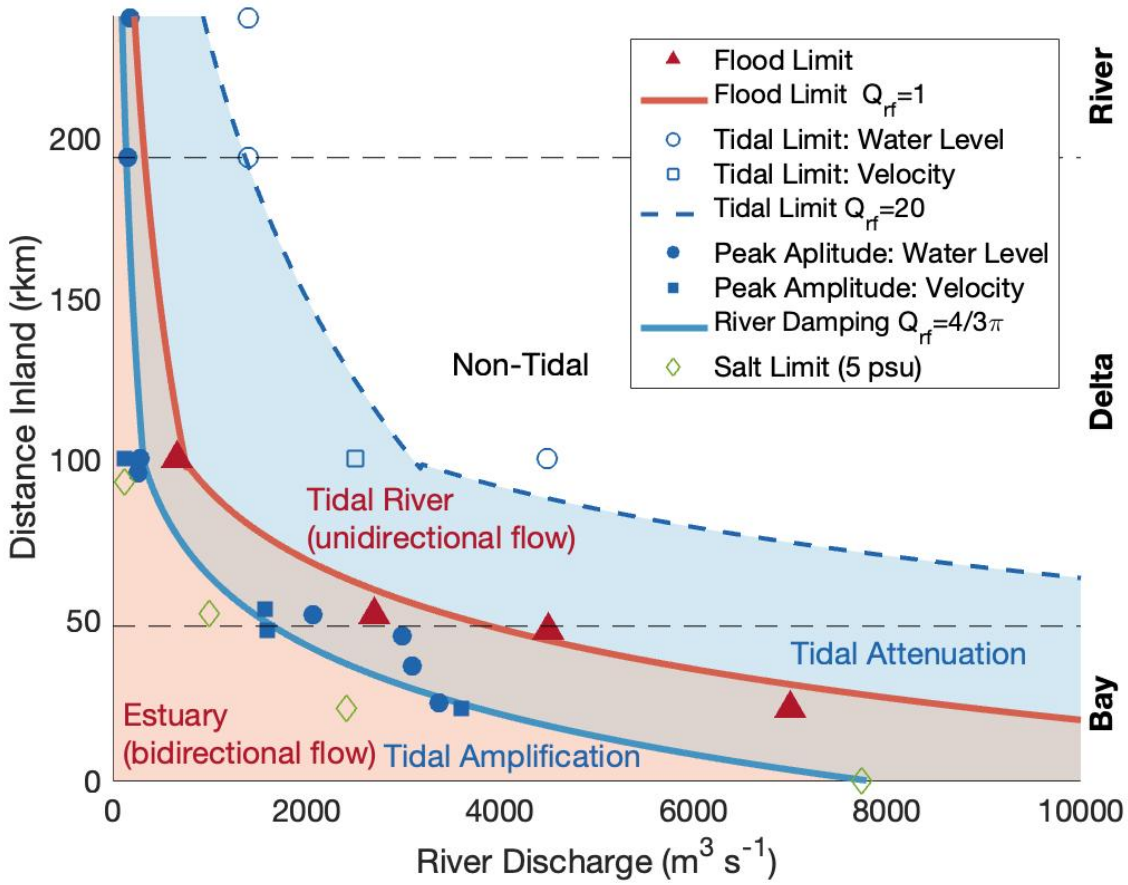

Figure 9. Observations (symbols) and solutions (lines/fill) summarizing tide-river dynamics along the fluvial-marine transition. The primary effects of river discharge on tides are colored for flow direction (red) or amplitude (blue) and gradually shift seaward as river discharge increases. The red fill captures the longitudinal region with bidirectional flow and is the tidal estuary, while the region without red fill is unidirectional and a tidal river where tides persist. The blue fill captures the longitudinal region where river flow attenuates tides and is contrasted with the seaward region where river induced stratification amplifies tides and the landward region where tides are damped. The overlapping purple region captures the low energy area where reversing tides attenuate from river flow. The flood limit was approximated using a Q_{rf} value based on figure S2a. The 5psu salinity limit is from Dykstra & Dzwonkowski (2020) when river discharge is increasing and remains just seaward of river damping and peak tidal amplitudes.